Author Contributions:

Conceptualization: Yuming Jin, Ralph F. Keeling
Data curation: Britton B. Stephens, Eric J. Morgan
Formal analysis: Yuming Jin, Britton B. Stephens
Funding acquisition: Britton B. Stephens, Ralph F. Keeling
Investigation: Yuming Jin
Methodology: Yuming Jin, Britton B. Stephens, Eric J. Morgan

Seasonal Tropospheric Distribution and Air-Sea Fluxes of Atmospheric Potential Oxygen From Global Airborne Observations

Yuming Jin[1] , Britton B. Stephens[2] , Ralph F. Keeling[1] , Eric J. Morgan[1] , Christian Rödenbeck[3] , Prabir K. Patra[4] , and Matthew C. Long[2]

[1]Scripps Institution of Oceanography, University of California, San Diego, La Jolla, CA, USA, [2]National Center for Atmospheric Research, Boulder, CO, USA, [3]Max Planck Institute for Biogeochemistry, Jena, Germany, [4]Research Institute for Global Change, Japan Agency for Marine-Earth Science and Technology, Yokohama, Japan

Abstract Seasonal change of atmospheric potential oxygen (APO $\sim O_2 + CO_2$) is a tracer for air-sea O_2 flux with little sensitivity to the terrestrial exchange of O_2 and CO_2. In this study, we present the tropospheric distribution and inventory of APO in each hemisphere with seasonal resolution, using O_2 and CO_2 measurements from discrete airborne campaigns between 2009 and 2018. The airborne data are represented on a mass-weighted isentropic coordinate ($M_{\theta e}$) as an alternative to latitude, which reduces the noise from synoptic variability in the APO cycles. We find a larger seasonal amplitude of APO inventory in the Southern Hemisphere relative to the Northern Hemisphere, and a larger amplitude in high latitudes (low $M_{\theta e}$) relative to low latitudes (high $M_{\theta e}$) within each hemisphere. With a box model, we invert the seasonal changes in APO inventory to yield estimates of air-sea flux cycles at the hemispheric scale. We found a larger seasonal net outgassing of APO in the Southern Hemisphere (518 ± 52.6 Tmol) than in the Northern Hemisphere (342 ± 52.1 Tmol). Differences in APO phasing and amplitude between the hemispheres suggest distinct physical and biogeochemical mechanisms driving the air-sea O_2 fluxes, such as fall outgassing of photosynthetic O_2 in the Northern Hemisphere, possibly associated with the formation of the seasonal subsurface shallow oxygen maximum. We compare our estimates with four model- and observation-based products, identifying key limitations in these products or in the tools used to create them.

Plain Language Summary A better understanding of the air-sea O_2 fluxes facilitates the study of marine productivity, global carbon cycle and ocean heat transport. Seasonal air-sea exchange of O_2 has been estimated by combining precise measurements of atmospheric O_2 and CO_2 into atmospheric potential oxygen (APO $\sim O_2 + CO_2$). Using APO observations from nine global airborne campaigns between 2009 and 2018, we resolved the seasonal cycle of atmospheric APO concentration in multiple pressure and latitude bands, yielding estimates of the tropospheric APO inventory, and area-integrated air-sea APO flux of each hemisphere. To a first approximation, the ocean is a source of APO in the spring and summer but a sink in the fall and winter, tracking the seasonal warming and cooling of the ocean as well as different ocean biogeochemistry and ventilation regimes. In addition, these cycles show clear asymmetry between hemispheres and display a progressive shift in the seasonal phase and amplitude across latitudes. It is therefore important to understand the physical and biogeochemical processes that lead to these differences.

1. Introduction

Atmospheric potential oxygen (APO), which is effectively the sum of atmospheric O_2 and CO_2 concentrations, is primarily a tracer of ocean biogeochemistry (Stephens et al., 1998). APO is generally insensitive to photosynthesis and respiration of the land biosphere due to compensating impacts on O_2 and CO_2. APO has been observed at surface stations (e.g., Battle et al., 2006; Goto et al., 2017; Manning & Keeling, 2006; Tohjima et al., 2003, 2019), on ship transects (Ishidoya et al., 2016; Pickers & Manning, 2015; Pickers et al., 2017; Stephens et al., 2011; Thompson et al., 2007; Tohjima et al., 2012, 2015), and from aircraft (Bent, 2014; Ishidoya et al., 2022; Langenfelds, 2002; Stephens et al., 2021). A prominent feature in time series of APO are seasonal variations, driven mainly by seasonal air-sea O_2 flux due to upper-ocean biological activities, thermally induced solubility changes, and ocean ventilation, with smaller contributions from air-sea exchanges of CO_2 and N_2 (Manning & Keeling, 2006; Stephens et al., 1998). APO is also sensitive to the burning of petroleum and natural gas, which are

Project Administration: Ralph F. Keeling
Resources: Britton B. Stephens, Christian Rödenbeck, Prabir K. Patra, Matthew C. Long
Software: Christian Rödenbeck, Prabir K. Patra, Matthew C. Long
Supervision: Ralph F. Keeling
Validation: Yuming Jin
Visualization: Yuming Jin
Writing – original draft: Yuming Jin, Ralph F. Keeling
Writing – review & editing: Yuming Jin, Britton B. Stephens, Ralph F. Keeling, Eric J. Morgan, Christian Rödenbeck, Matthew C. Long

characterized by more negative O_2:C ratios than land photosynthesis/respiration, but combustion of these products make a negligible contribution to seasonal APO cycles at background stations (Manning & Keeling, 2006; Nevison et al., 2008).

Measurements of seasonal variations in atmospheric APO have been used to estimate oceanic net community production (NCP) (Goto et al., 2017; Nevison et al., 2012, 2018), evaluate the ocean biogeochemistry components of Earth System Models (Naegler et al., 2007; Nevison et al., 2015, 2016; Stephens et al., 1998), and estimate gas-exchange velocities (R. F. Keeling et al., 1998). These measurements have also been used to validate estimates of climatological seasonal air-sea O_2 flux, which are calculated based on measurements of dissolved O_2 in the surface ocean (Garcia & Keeling, 2001; Keeling et al., 1998; Najjar & Keeling, 1997, 2000). Atmospheric APO observations have also been inverted to yield global air-sea APO fluxes that are optimized to best match observed APO at surface stations, thus constraining global-scale seasonal air-sea O_2 exchange (Rödenbeck et al., 2008). The accuracy of air-sea O_2 fluxes inferred from atmospheric measurements is limited, however, by uncertainties due to vertical transport in atmospheric tracer transport models as well as by the limited coverage of atmospheric measurements (Naegler et al., 2007; Nevison et al., 2008).

Here we use APO measurements from two global airborne campaigns, the HIAPER Pole-to-Pole Observations (HIPPO) project (S. C. Wofsy, 2011) and the Atmospheric Tomography (ATom) mission (Thompson et al., 2022), to quantify climatological seasonal APO distributions, tropospheric inventories, and air-sea fluxes at the hemispheric scale. The APO seasonal cycles are expressed on a mass-weighted moist isentropic coordinate, $M_{\theta e}$, developed by Y. Jin et al. (2021), which is an alternative to latitude and effectively removes the impact of synoptic variability from airborne data. Due to the known tendency for rapid adiabatic airmass mixing (mixing along moist isentropes) (Parazoo et al., 2011; Pauluis et al., 2008), long-lived atmospheric tracers such as O_2 and CO_2 tend to be well-mixed on $M_{\theta e}$ (or θ_e), which allows hemispheric inventories to be estimated by a simple one-dimensional integration over $M_{\theta e}$. We use this method to generate hemispheric inventories of APO. We then invert these inventories using a box model to yield hemispheric scale air-sea APO fluxes. We apply our estimates as a direct test to other model and observation-based products, such as the Jena CarboScope APO inversion (Rödenbeck et al., 2008), climatological Garcia and Keeling (2001) O_2 fluxes from a heat flux based extension of dissolved O_2 measurements, and one configuration of the Community Earth System Model (CESM, Yeager et al., 2022).

2. Materials and Methods

2.1. Definition of APO and Air-Sea APO Fluxes

Following Stephens et al. (1998), APO (per meg) is calculated from observations according to

$$\text{APO} = \delta(O_2/N_2) + \frac{1.1}{X_{O_2}}(CO_2 - 350) \tag{1}$$

with

$$\delta(O_2/N_2) = \left(\frac{\left(\frac{O_2}{N_2} \right)_{\text{sample}}}{\left(\frac{O_2}{N_2} \right)_{\text{reference}}} - 1 \right) \cdot 10^6 \tag{2}$$

where 1.1 is the approximate exchange ratio of O_2 production/consumption to CO_2 consumption/production from terrestrial biosphere (Severinghaus, 1995). We note that this ratio is generally between 1.01 and 1.14 from aboveground carbon pool over small temporal and spatial scales (Gallagher et al., 2017; Hockaday et al., 2009; Worrall et al., 2013). For this study, the relevant ratio is that of O_2 to CO_2 in the seasonally accumulated growth and decay of hemispheric biota, which we assume to be 1.1 following the stoichiometric and biological arguments in Severinghaus, 1995. Sensitivity results over the range of 1.1 ± 0.05 show only minor effects (±5.1% of the hemispheric average APO, for details see Text S2.4 in Supporting Information S1), as seasonal APO changes are dominated by seasonal changes in $\delta(O_2/N_2)$. $\delta(O_2/N_2)$ is conventionally multiplied by 10^6 and expressed in per meg units, and ΔCO_2 is the difference in the CO_2 dry-air mole fraction in ppm (i.e., μmol mol^{-1}) relative to a reference of 350 ppm. Here X_{O_2} (0.2094) is the reference dry-air mole fraction of O_2 used in the definition of the

O_2/N_2 scale of the Scripps O_2 Program (Keeling et al., 2020). The unit of APO can be converted from per meg to ppm equivalent for flux contributions by multiplying X_{O_2}.

The seasonal cycle of atmospheric APO is altered by oceanic emission or uptake of O_2, CO_2, or N_2. We define the oceanic flux of APO ($F^{APO(ocn)}$, Tmol day^{-1}) following:

$$F^{APO(ocn)} = \left(F^{O_2} + 1.1 F^{CO_2} - \frac{X_{O_2}}{X_{N_2}} F^{N_2} \right) \times A \tag{3}$$

where F^{O_2}, F^{CO_2}, and F^{CO_2} are air-sea flux of O_2, CO_2, and N_2, in unit of Tmol m^{-2} day^{-1}, and A is the ocean area, in unit of m^2. X_{N_2} (0.7808) is the reference dry-air mole fraction of N_2 in the atmosphere (Keeling et al., 2020). We also define the change in APO inventory as the change in the total abundance of APO (in Tmol) in a defined atmospheric volume. In a well-mixed atmospheric volume, the excess APO inventory in moles (relative to reference air) is equal to APO $\cdot X_{O_2} \cdot M \cdot 10^{-6}$, where M is the total moles of dry air in the volume.

2.2. Airborne Campaigns and Airborne APO Measurements

Both the HIPPO and ATom campaigns had global coverage (Figure 1a, Table S1 in Supporting Information S1), extending from the Arctic to the Antarctic and near the surface (150–300 m) to the lower stratosphere (12–15 km) (Thompson et al., 2022; S. C. Wofsy, 2011). HIPPO consisted of five campaigns between 2009 and 2011 and ATom consisted of four campaigns between 2016 and 2018. Each campaign included a southbound and a northbound transect. On HIPPO, both southbound and northbound transects were over the Pacific Ocean, while on ATom, southbound transects were over the Pacific Ocean and northbound transects were over the Atlantic Ocean. We aggregate data from each mission into southbound and northbound transects within each hemisphere.

This study uses airborne measurements of $\delta(O_2/N_2)$ and CO_2 made with the NCAR Airborne Oxygen Instrument (AO2) (Stephens et al., 2021). The AO2 instrument was supported by flask samples collected with the NCAR/Scripps Medusa flask sampler that collects 32 air samples in each flight for later analysis at Scripps (Bent, 2014; Stephens et al., 2021). The Medusa flasks were used to identify and correct time-dependent systematic biases in the continuous AO2 measurements. AO2 data were adjusted to match Medusa flask using a linear trend versus time of flight on a flight-by-flight average basis (Stephens et al., 2021). O_2 measurements were adjusted for surface effects and detector cell humidity interactions, while CO_2 measurements were adjusted for surface effects and o-ring permeation effects (Stephens et al., 2021). The magnitude of O_2 adjustments for each campaign is listed in Table S3 of Stephens et al. (2021), while the magnitude of CO_2 adjustments per campaign ranges from -0.3 to 0.4 ppm, with an average of 0.01 ppm and 1σ standard deviation of 0.19 ppm. Prior to being used for correcting the AO2 measurements, the Medusa data were also adjusted to reduce the impact of diffusive fractionation associated with flask sampling (Bent, 2014; Stephens et al., 2021) by computing

$$\delta \left(\frac{O_2}{N_2} \right)^* = \delta \left(\frac{O_2}{N_2} \right)_{obs} - \frac{1}{3.77} \delta \left(\frac{Ar}{N_2} \right)_{obs} \tag{4}$$

where $\delta(O_2/N_2)_{obs}$ is the Medusa observation, and $\delta(Ar/N_2)_{obs}$ is measured relative to an arbitrary reference of 15 per meg chosen to approximate the global surface average (Stephens et al., 2021). 3.77 is the ratio of the Ar/N_2 change to O_2/N_2 change associated with thermal fractionation (Bent, 2014; Keeling et al., 2004). This correction recognizes that

$$\delta \left(\frac{O_2}{N_2} \right)_{obs} = \delta \left(\frac{O_2}{N_2} \right) + \delta \left(\frac{O_2}{N_2} \right)_{fract} \tag{5}$$

$$\delta \left(\frac{Ar}{N_2} \right)_{obs} = \delta \left(\frac{Ar}{N_2} \right) + \delta \left(\frac{Ar}{N_2} \right)_{fract} \tag{6}$$

with

$$\delta \left(\frac{O_2}{N_2} \right)_{fract} = \frac{1}{3.77} \delta \left(\frac{Ar}{N_2} \right)_{fract} \tag{7}$$
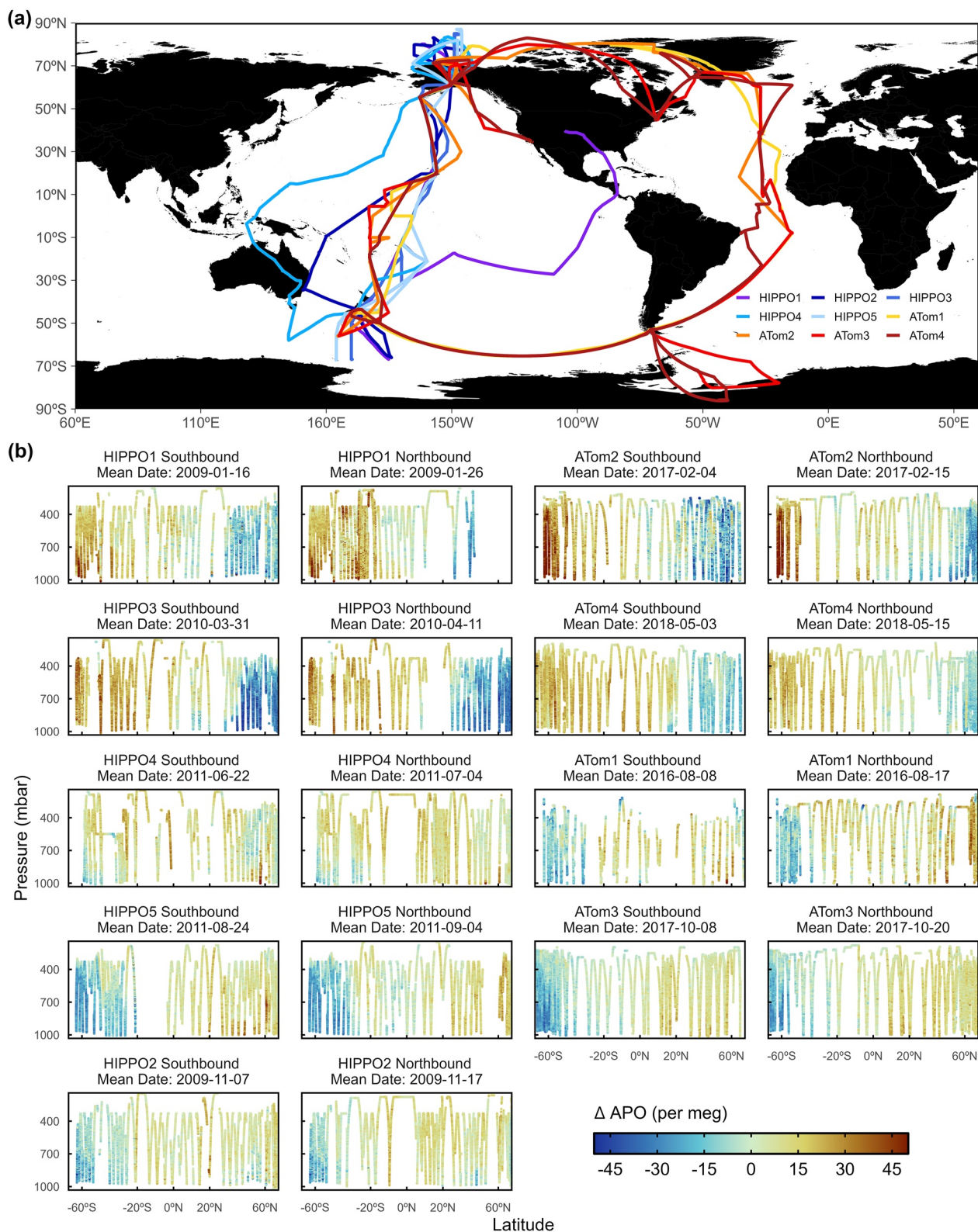
Figure 1. (a) HIPPO and ATom flight tracks colored by campaigns. (b) Latitude and pressure cross-sections of ΔAPO for each airborne campaign transect. Panels are ordered over the course of the season.

where the *obs* subscript denotes the observed value and the *fract* subscript denotes sampling artifacts caused by thermal fractionation at the air intake or flask exit port, which we expect are the dominant sampling artifacts. Pressure-driven inlet fractionation was also apparent, but with a small enough magnitude and similar enough expected ratio to be included in a single correction (Section 4.2.1 of Stephens et al., 2021).

The Medusa-corrected AO2 data are thus effectively measuring $\delta(O_2/N_2)^*$ on a mean basis per flight, from which we can compute

$$APO^* = \delta\left(\frac{O_2}{N_2}\right)^* + \frac{1.1}{X_{O_2}}(CO_2 - 350) \tag{8}$$

To calculate seasonal APO from APO*, it is necessary to correct for the true $\delta(Ar/N_2)$ seasonality. Here we use modeled estimates, which we refer to as $\delta(Ar/N_2)_{model}$, and assume that $\delta(Ar/N_2)_{model} = \delta(Ar/N_2)_{true}$. The $\delta(Ar/N_2)_{model}$ is calculated from simulated air-sea N_2 exchange based on scaling ocean heat flux. Thus

$$APO = APO^* + \frac{1}{3.77}\delta\left(\frac{Ar}{N_2}\right)_{model} \tag{9}$$

with

$$\begin{aligned}\delta\left(\frac{Ar}{N_2}\right)_{model} &= \frac{1}{X_{Ar}}\Delta Ar - \frac{1}{X_{N2}}\Delta N_2 \\ &= \frac{1}{X_{Ar}}\frac{1}{34}\Delta N_2 - \frac{1}{X_{N2}}\Delta N_2 \\ &= 1.87 \cdot \Delta N_2 \end{aligned} \tag{10}$$

where ΔN_2 is the modeled atmospheric N_2 anomaly driven by air-sea N_2 exchange, calculated as if N_2 were a trace gas in ppm-equivalent units (e.g., μmol mol^{-1}). X_{Ar} (0.00934) is the mole fraction of Ar in the atmosphere. 1/34 is a scaling factor, which is the ratio of Ar and N_2 air-sea fluxes driven by heat flux from Table 3 in Manizza et al. (2012). Air-sea N_2 exchange (F^{N_2}) is calculated from ocean heat fluxes (Q) from the Estimating the Circulation and Climate of the Ocean (ECCO) Version 4 Release 3, which interpolates ocean heat flux estimates to a global field by a non-linear inverse model (Forget et al., 2015)

$$F^{N_2} = -\frac{1}{1.3} \cdot \frac{dS}{dT} \cdot \frac{Q}{C_p} \tag{11}$$

where dS/dT (mol kg^{-1} C^{-1}) is the temperature derivative of solubility (Weiss, 1970), Q is the ocean heat flux (W m^{-2}) and C_p is the specific heat capacity of seawater (3993 J kg^{-1} C^{-1}). Equation 11 is similar to that used by Keeling and Shertz (1992) but with the introduction of the factor of 1/1.3 by X. Jin et al. (2007). This factor accounts for incomplete equilibration and other processes, including mixing-induced super-saturation due to the non-linear dependence of solubility on temperature and the penetration of solar radiation below the ocean mixed layer (Dietze & Oschlies, 2005; Manizza et al., 2012). We estimate ΔN_2 by forward transporting ECCO-based air-sea N_2 exchange using the TM3 atmospheric transport model (Heimann & Körner, 2003).

The difference between APO and APO* is small, ranging from −4 to 4 per meg (Figure S1 in Supporting Information S1). This correction also has a small impact on the seasonal amplitude of the APO concentrations, which scales up the seasonal amplitude of APO* by 0.89 per meg (4.7%) and 1.38 per meg (4.9%) in the Northern and Southern Hemisphere, respectively.

2.3. Filtering and Detrending of APO Airborne Observations

We exclude all measurements from the stratosphere using the criterion of Y. Jin et al. (2021): {Water vapor (H_2O) < 50 ppm} and {O_3 > 150 ppb or N_2O < 319 ppb}, where N_2O has detrended relative to a reference year of 2009. H_2O was measured using VCSEL (Zondlo et al., 2010) for HIPPO and DLH for ATom (Diskin et al., 2002; Scott et al., 1990). O_3 was measured by the NOAA Unmanned Aerial Systems Chromatograph for Atmospheric Trace Species (UCATS, Hintsa et al., 2021). N_2O was measured by the Harvard Quantum Cascade Laser System (QCLS, Santoni et al., 2014). N_2O measurements are not available from ATom1, so the stratosphere samplings

are simply defined by H_2O and O_3 for this campaign. We also exclude all observations near landing sites with the same criteria as in Y. Jin et al. (2021), for example, samples that were collected 120s after takeoff, 600s prior to landing, and any missed approaches.

To focus on APO seasonal cycles, we detrend the airborne measurements by subtracting a smoothed interannual trend from a global mean APO time series using data from the Scripps O_2 Program (Hamme & Keeling, 2008). This APO time series is calculated as a weighted average of APO measurements from seven surface stations, with the weights based on the latitudinal coverage of each corresponding station (Table S3 in Supporting Information S1, weights are from Hamme and Keeling (2008)). Smoothing was based on a least-squares fit consisting of a stiff cubic spline function plus 4-harmonic terms (Manning & Keeling, 2006; Reinsch, 1967). Detrended APO is referred to as ΔAPO. The latitude and pressure cross section of ΔAPO for each airborne campaign transect are shown in Figure 1b.

2.4. Air-Sea APO Flux Products

We compare airborne-based estimates of seasonal air-sea APO fluxes with four alternate estimates.

The first product uses APO fluxes from the Jena CarboScope APO Inversion (referred to as the Jena inversion, version: apo99XS_v2022), which yields APO fluxes optimized to best match observed APO at stations in the Scripps O_2 Program surface flask network and at stations and on ships (Tohjima et al., 2012) from the National Institute for Environmental Studies (updates of Rödenbeck et al., 2008). Details of stations and their locations are in Table S2 in Supporting Information S1. We use the fluxes from 2009 to 2018, to match with the duration of the HIPPO and ATom campaigns.

The second product is an observation-based semi-empirical product (referred to as GKT), using year-to-year repeating climatological F^{O_2} from Garcia and Keeling (2001), climatological F^{CO_2} from Takahashi et al., 2009, and climatological F^{N_2} calculated from ocean heat fluxes from ECCO version 4 (see Section 2.2, Forget et al., 2015). F^{O_2} from Garcia and Keeling (2001) is calculated by interpolating dissolved O_2 measurements weighted by ocean heat flux anomalies. Following Morgan et al. (2021), here we scale down the F^{O_2} by 18% (i.e., multiply by a factor of 0.82) to accounts for bias in the gas transfer velocity from Wanninkhof (1992), which is used to calculate F^{O_2} from Garcia and Keeling (2001). Naegler et al. (2006) showed that the gas transfer velocity coefficient of 0.39 from Wanninkhof (1992) should be scaled down by 18% to 0.32. This scaling is also supported by Bent (2014).

The third product is based on a forced ocean-ice configuration of CESM2 (Yeager et al., 2022, referred to as CESM), which is forced by JRA55-do (Tsujino et al., 2018) atmospheric fields and prognostic ocean BGC using the Marine Biogeochemistry Library (MARBL; Long et al., 2021). The oceanic O_2 (F^{O_2}), CO_2 (F^{CO_2}) and N_2 (F^{N_2}) fluxes are provided directly as model output, with $1° \times 1°$ horizontal resolution and daily resolution from 1986 to 2020. We only analyze outputs from 2009 to 2018.

We calculate area-integrated daily air-sea APO flux cycles in each hemisphere from these three products, and fit with a 2-harmonic plus offset to yield average seasonal cycles (Figure 5). We note that the GKT is defined as a seasonal anomaly, so the annual uptake is pre-subtracted (equal to 0).

2.5. Atmospheric Simulations

To translate APO fluxes from these products into atmospheric distributions, we rely on the TM3 transport model (Heimann & Körner, 2003) and MIROC4.0-based Atmospheric Chemistry-Transport Model (ACTM, Patra et al., 2018). TM3 was run at a 5° longitude by 4° latitude spatial resolution with 19 vertical levels, using winds from NCEP/NCAR reanalysis with daily temporal resolution (Kalnay et al., 1996). With the modeled fluxes as input, the TM3 model yields as output excesses or deficits of APO against a prescribed background. The simulated APO atmospheric fields are referred to as Jena-TM3, GKT-TM3, and CESM-TM3. These simulations were run from 2006 to 2018. The first 3 years are used for model spin-up and are discarded. We use the model output from 2009 to 2018.

We also use ACTM to forward transport air-sea APO fluxes from the Jena APO inversion (referred to as Jena-ACTM), in order to provide another constraint on interhemispheric-mixing time scales (for details see
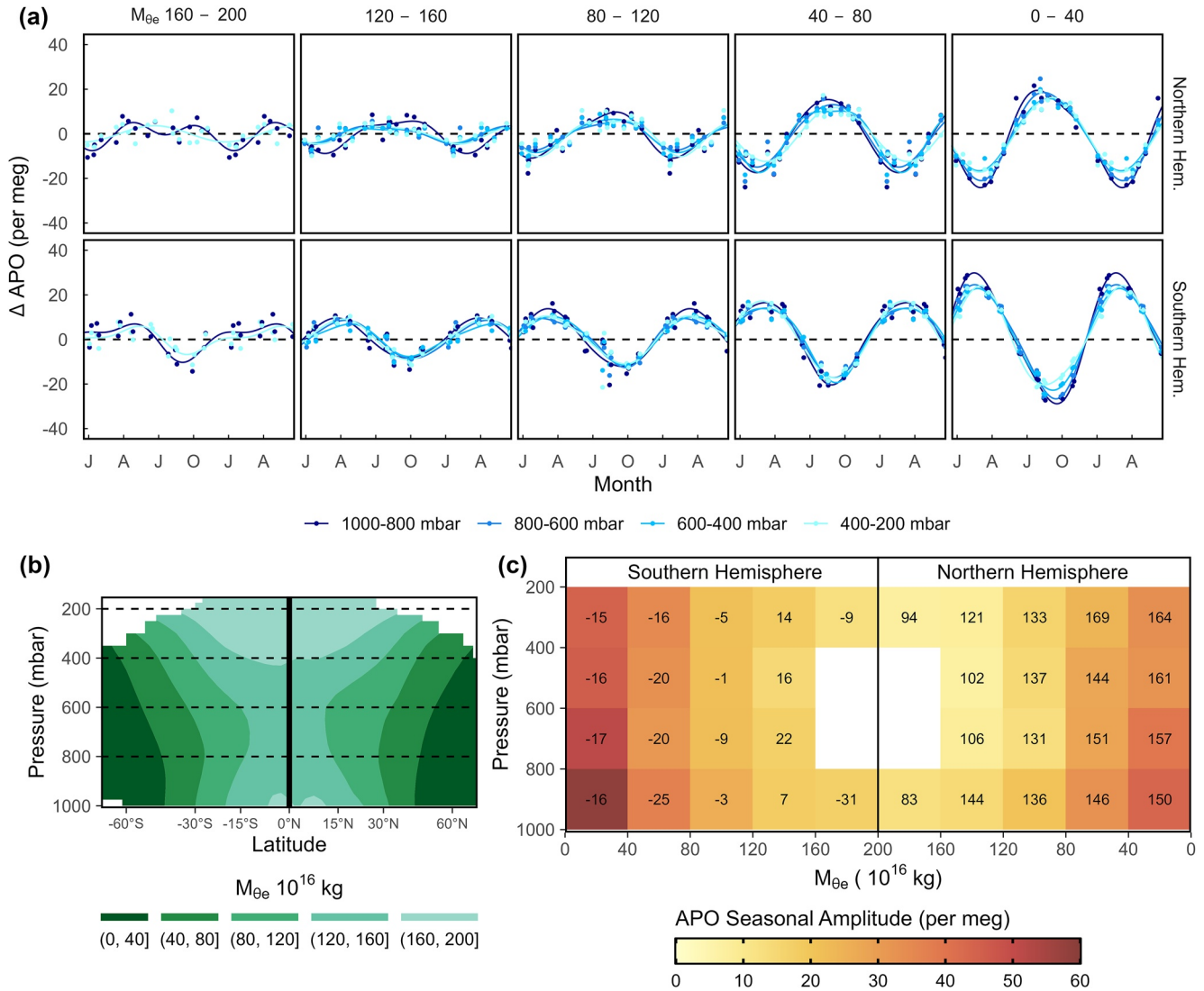
Figure 2. (a) Seasonal cycles of detrended airborne APO (ΔAPO) sorted by $M_{\theta e}$–pressure bins (columns) and hemispheres (rows). $M_{\theta e}$ bins (10^{16} kg) are shown at the top of each panel and pressure bins are colored. Each point represents the mass-weighted average (based on $M_{\theta e}$) ΔAPO within the specific $M_{\theta e}$–pressure bins, filtering out bins with less than 20 10-s observations. The curves represent two-harmonic fits to the corresponding mass-weighted average ΔAPO of each $M_{\theta e}$ and pressure bin. Annul mean values are subtracted. The first half year is repeated in each panel. Bins in the mid-troposphere (800–600 mbar and 600–400 mbar) of the highest $M_{\theta e}$ value (160–200) are dropped because these bins contain very little air mass. (b) Schematic of the contours of zonal and annual average $M_{\theta e}$ in the Latitude-Pressure coordinate, calculates as the average $M_{\theta e}$ in the year of 2009 using ERA-Interim. (c) Seasonal amplitude (shading) and phase (upward zero-crossing Julian date) of the fitted APO seasonal cycles in (a). Negative Julian dates are given from November to December. Bins in the mid-troposphere (800–600 mbar and 600–400 mbar) of the highest $M_{\theta e}$ value (160–200) are dropped because these bins contain very little air mass.

Section 5.1 and Appendix A). ACTM was run from 1999 to 2019 at ~2.8° longitude by ~2.8° latitude spatial resolution with 67 vertical levels driven by JRA-55 winds (Kobayashi et al., 2015). We only used Jena-ACTM output between 2009 and 2018.

2.6. Calculation of $M_{\theta e}$ and $M_{\theta e}$-Weighted Average APO

Airborne APO observations are sorted and binned on the $M_{\theta e}$ coordinate, which is defined as the total dry air mass under a specific moist isentropic value (defined by constant θ_e) in the troposphere of each hemisphere (Y. Jin et al., 2021). $M_{\theta e}$ is defined separately in the Northern and Southern Hemispheres and is not continuous across the Equator. The coordinate $M_{\theta e}$ is similar to θ_e, generally increasing toward the equator and with altitude in each hemisphere (Figure 2b). The computation of $M_{\theta e}$ follows:

$$M_{\theta_e}(\theta_e, t) = \sum M_x(t)\big|_{\theta_{ex} < \theta_e} \qquad (12)$$

where $M_x(t)$ is the dry air mass of each grid cell x at time t, and θ_{ex} is the equivalent potential temperature. The sum is over all air with θ_{ex} less than θ_e in the troposphere, which is defined as PVU smaller than 2. This calculation yields a unique value of M_{θ_e} for each value of θ_e. We refer to the relationship between θ_e and M_{θ_e} as the "θ_e-M_{θ_e} look-up table," which we generate at the daily resolution for each hemisphere based on four reanalyses, which are ERA-Interim (Dee et al., 2011), MERRA-2 (Gelaro et al., 2017), NCEP (Kalnay et al., 1996), and JRA-55 (Kobayashi et al., 2015). We use a look-up table based on ERA-Interim to organize airborne data. These look-up tables are available at https://doi.org/10.5281/zenodo.4420398.

The M_{θ_e} value for each airborne observation was derived by matching the θ_e value of each observation with the ERA-Interim look-up table of the corresponding date.

We calculate θ_e (K) following Stull (2012):

$$\theta_e = \left(T + \frac{L_v(T)}{C_{pd}} w \right) \left(\frac{P_0}{P} \right)^{\frac{R_d}{C_{pd}}} \qquad (13)$$

where w is the water vapor mixing ratio with a unit of kg of water vapor per kg of air mass, R_d (287.04 J kg^{-1} K^{-1}) is the gas constant for air, C_{pd} (1005.7 J kg^{-1} K^{-1}) is the specific heat of dry air at constant pressure, P_0 (1013.25 mbar) is the reference pressure at the surface, and $L_v(T)$ (kJ kg^{-1}) is the latent heat of evaporation. $L_v(T)$ is defined as 2406 kJ kg^{-1} at 40 °C and 2501 kJ kg^{-1} at 0 °C and scales linearly with temperature.

For HIPPO, θ_e is available from the merged file that is calculated using the water vapor mole fraction measured by VCSEL (Zondlo et al., 2010). For ATom, θ_e was computed from static pressure, air temperature as measured by the Meteorological Measurement System (MMS), and relative humidity of water vapor as measured by the Diode Laser Hygrometer (DLH) (Diskin et al., 2002; Scott et al., 1990).

We also assign a M_{θ_e} value for each grid of the modeled daily atmospheric APO field (TM3 and ACTM) using 3-D atmospheric M_{θ_e} fields derived from the corresponding reanalysis used in the transport model. 3-D M_{θ_e} fields are interpolated to the transport model grids using inverse distance weighted interpolation.

To calculate the mass-weighted average detrended APO for a given M_{θ_e} band, we use a method that assumes each APO observation represents the APO value on the corresponding M_{θ_e} surface throughout the hemisphere (Y. Jin et al., 2021). We sort APO by M_{θ_e} from low to high and compute a mass-weighted average APO by trapezoidal integration of APO as a function of M_{θ_e}, dividing by the range of M_{θ_e}. This method effectively weighs each measurement or modeled value by the fraction of the hemispheric airmass with the same θ_e value that it represents. The method yields accurate inventories because, as shown below, the variability in APO along M_{θ_e} surfaces is small due to rapid adiabatic mixing (see also Y. Jin et al., 2021), and because this variability is also partly addressed by averaging data from different elevations.

3. Seasonal Atmospheric APO Distributions

We examined the seasonal cycle of airborne APO grouped into five M_{θ_e}-pressure bins (40 × 10^{16} kg intervals) in each hemisphere and four pressure bins (200 mbar intervals), as shown in Figure 2a. The approximate geographic distribution of each bin is illustrated by the zonal average M_{θ_e} surfaces in Figure 2b. These cycles are calculated by 2-harmonic fits (with offset removed) to each averaged Δ APO of the M_{θ_e} and pressure bin (shown as points in Figure 2a). Statistics of the cycles (amplitude and phase) in the different bins are summarized in Figure 2c. A comparison of observed cycles and simulated cycles (i.e., Jena-TM3, GKT-TM3, and CESM-TM3) grouped by 20 (10^{16} kg) M_{θ_e} intervals is shown in Figure S2 in Supporting Information S1.

In Figure 2a, all bins show well-resolved seasonal APO cycles with higher amplitudes in the Southern Hemisphere compared to the Northern Hemisphere at a given pressure-M_{θ_e} bin. Within each hemisphere, the amplitudes show a clear gradient across M_{θ_e}, with larger amplitudes at lower M_{θ_e} (higher latitudes). Phasing of the APO cycles also shows clear gradients over M_{θ_e}. While the cycles within the Southern Hemisphere have earlier phasing (upward zero-crossing date) at low M_{θ_e} (high latitude), the cycles in the Northern Hemisphere tend to have later

phasing at low $M_{\theta e}$. These patterns in amplitude and phase are similar to those seen in summaries of surface or shipboard measurements (Keeling et al., 1998; Tohjima et al., 2012).

In a given $M_{\theta e}$ bin (Figures 2a and 2c), the amplitude decreases slightly with increasing altitude (decreasing pressure) due to the fact that surface fluxes drive the APO seasonal cycle. The weak variation with pressure (at constant $M_{\theta e}$) is expected considering that θ_e (or $M_{\theta e}$) surfaces are preferential surfaces for mixing. The phase generally shifts later with decreasing pressure, consistent with a time lag for adiabatic mixing of the APO cycle along θ_e surfaces. An exception to this pattern is seen in the high $M_{\theta e}$ (120–160) bins of the Northern Hemisphere, where the earliest phase is found in the mid-troposphere (800–400 mbar), while the lower (1,000–800 mbar) and upper troposphere (400–200 mbar) show clear lags in phase (Figure 2a).

The gradients in seasonal phasing with respect to $M_{\theta e}$ are mainly driven by fluxes at higher latitudes in each hemisphere and are partly driven by delayed propagation of the cycles from the opposite hemisphere (Garcia & Keeling, 2001; Keeling et al., 1998; Najjar & Keeling, 2000). These effects, together with the ~180° out-of-phase seasonal flux cycle between low-latitudes (<20°N) and high-latitudes in the Northern Hemisphere (Figure S7 in Supporting Information S1), lead to the small and noisy seasonal cycle of the highest $M_{\theta e}$ band (low latitude) in the Northern Hemisphere. We find that the upward zero-crossing date arrives ~5.5 weeks earlier in the high $M_{\theta e}$ (120–160) of the northern mid-troposphere (800–600 mbar) relative to the lower troposphere (1,000–800 mbar), as shown in Figures 2a and 2c. This pattern is consistent with Keeling et al. (1998), who found that the observed seasonal maximum at the Mauna Loa Observatory (MLO, 3397 masl) is 2 months earlier than the seasonal maximum at Cape Kumukahi (KUM, 15 masl), which is only 82 km from MLO, but at a lower elevation.

As an alternative, we also have binned airborne observations by pressure and latitude (Figure S3b in Supporting Information S1). This approach leads to a much larger scatter of amplitudes and phases in APO seasonal cycles with pressure level (at fixed latitude bins) compared to binning data using pressure and $M_{\theta e}$ (Figure 2a and Figure S3a in Supporting Information S1). A larger scatter is expected, which illustrates the advantage of organizing airborne observations on $M_{\theta e}$. Binning airborne observations by pressure and latitude also leads to larger short-term variability (F test, $p < 0.01$) within individual pressure bins relative to the mean cycles, based on the distribution of all detrended observations (not shown as points but denoted as 1σ values in Figure S3 in Supporting Information S1), indicating larger synoptic disturbances.
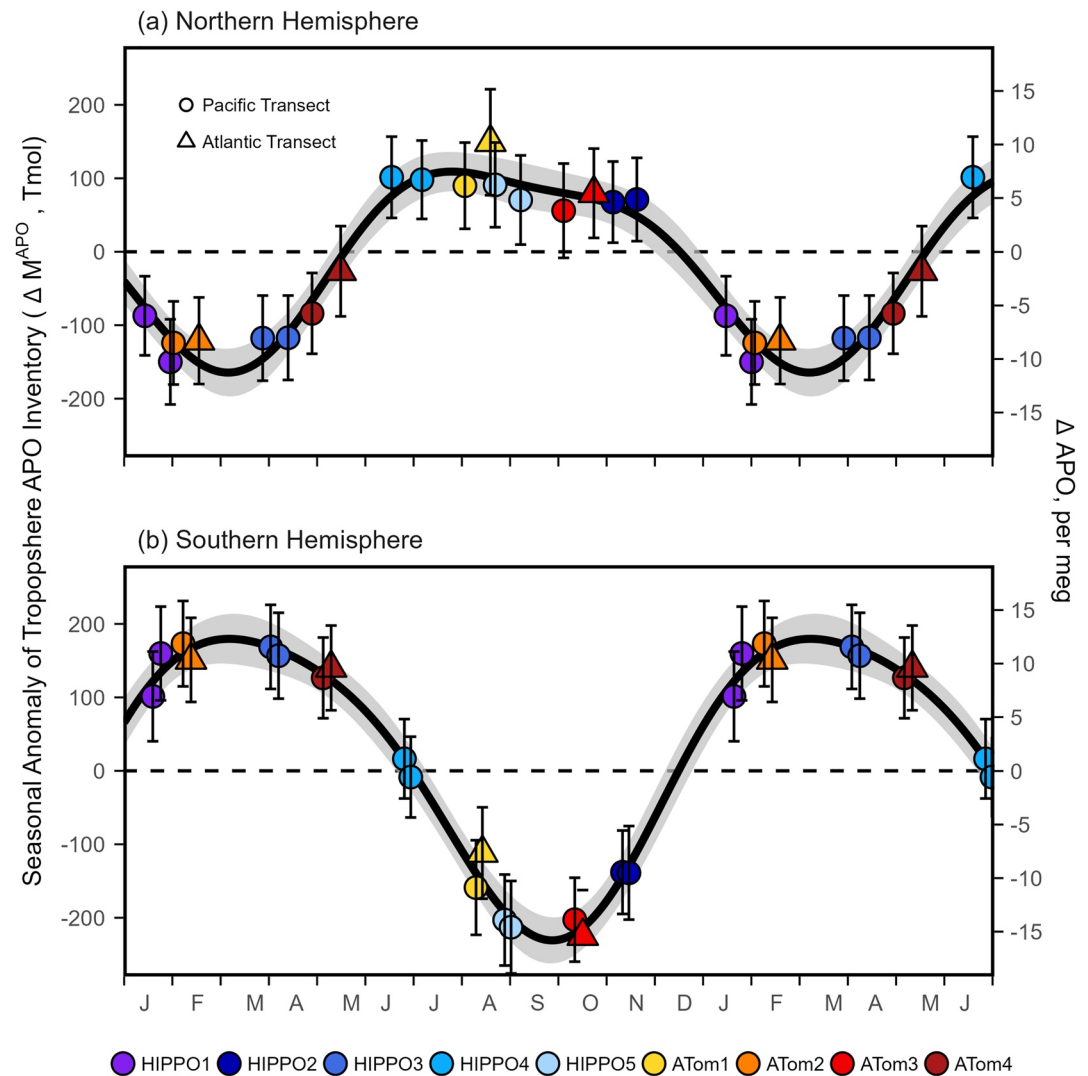
4. Seasonal Cycles of Tropospheric APO Inventories

4.1. Method

We show our estimates of APO inventory seasonal anomalies (ΔM^{APO}) of each airborne campaign transect in Figure 3, and their values are reported in Table S4 and S5 in Supporting Information S1, including uncertainties. Inventory estimates from different years are grouped into a climatological year. For each of the 18 airborne transects, we calculated mass-weighted average detrended APO ($\langle\Delta APO\rangle$) for each hemisphere. We then compute ΔM^{APO} (in moles) of each hemisphere from the hemispheric mass-weighted average Δ APO ($\langle\Delta APO\rangle$) as follows:

$$\Delta M^{APO} = \langle\Delta APO\rangle \cdot X_{O_2} \cdot M_{trop} \cdot \kappa \tag{14}$$

The parameter M_{trop} is the total tropospheric dry air mass of the hemisphere. Here we use a constant hemispheric dry air mass of $2.02 \cdot 10^{18}$ kg, which ensures that δM^{APO} is insensitive to changes in tropospheric air mass in the absence of changes in APO concentration. The total mass of dry air in the troposphere of each hemisphere is computed by integrating all ERA-Interim tropospheric (PVU < 2) grid cells. The changes in tropospheric air mass with season are small in any case, varying from $2.00 \cdot 10^{18}$ kg to $2.04 \cdot 10^{18}$ kg in the Southern Hemisphere and from $1.97 \cdot 10^{18}$ kg to $2.06 \cdot 10^{18}$ kg in the Northern Hemisphere. The parameter κ ($3.45 \cdot 10^{-17}$ Tmol kg^{-1}) is a constant that converts an amount of dry air mass from kg to Tmol, which consists of the product of $10^3/28.97$ (i.e., converts kg of air mass to mol of air mass), 10^{-12} (i.e., converts mol of air mass to Tmol of air mass) and 10^{-6} (i.e., converts ppm to mol/mol). Seasonal cycles of tropospheric APO inventory of each hemisphere are calculated by 2-harmonic fits with annual offset removed (Figure 3). Related statistics (seasonal amplitude, maximum and minimum date, upward zero-crossing date) based on 2-harmonic fits are summarized in Table 1.

The $M_{\theta e}$ integration method can yield unbiased tropospheric APO inventories if the spatial coverage of airborne measurements is broad enough (Y. Jin et al., 2021). Also, APO inventories for multiple campaigns can define

Figure 3. Seasonal anomaly of tropospheric APO inventory (Tmol) or concentration (per meg) in the Northern (a) and Southern (b) Hemispheres. Points show estimates of seasonal APO anomaly of each airborne campaign transect computed from the M_{θ_e} integration method (for details see Section 4.1), with annual mean removed using the value based on 2-harmonic fits to points. Error bars provide the overall uncertainty of each APO anomaly estimate (Text S2 in Supporting Information S1). Points from different years are grouped into a climatological year. Circles indicate transects over the Pacific Ocean, and triangles indicate transects over the Atlantic Ocean. Thick black lines represent 2-harmonic fits (annual mean removed) to corresponding seasonal APO anomaly estimates, with shaded region as 1σ uncertainty, which is calculated as the standard deviation of an ensemble of 2000 2-harmonic fits to points that incorporate uncertainty. The observed APO inventory estimates (points) are corrected for bias due to limited spatial and temporal coverage of airborne observations (Text S1 in Supporting Information S1). The first half-year is repeated.

climatological mean seasonal cycles only if their temporal coverage is sufficient. We assess the bias due to incomplete coverage by subsampling simulated 3-D fields of APO (from Jena-TM3 and Jena-ACTM, see Figure S4 in Supporting Information S1) as detailed in Text S1 in Supporting Information S1. This approach yields estimated errors for each airborne campaign transect on the corresponding mean day of year. We only find small errors, with an average RMSE across the 18 transects of 1.67 per meg (based on TM3) or 1.21 per meg (based on ACTM) in the Northern Hemisphere, and 1.42 per meg (based on TM3) or 1.68 per meg (based on ACTM) in the Southern Hemisphere, suggesting that the airborne data and M_{θ_e} integration method could represent hemispheric average APO well. We also find that the TM3 and ACTM models generally agree with the sign of biases (Figure S4 in Supporting Information S1). We use these calculated errors (averaged from TM3 and ACTM) to correct the observed APO inventory seasonal anomalies estimated from each airborne campaign

Table 1
Statistics of the Seasonal Cycle of Tropospheric APO Inventory (Figure 3) From Two-Harmonic Fits (Annual Mean Removed) for Each Hemisphere Computed From Airborne Observations With Correction for Sparse Spatial and Temporal Coverage

Product	Hemisphere	Seasonal amplitude (Tmol)	Maximum date	Minimum date	Upward-zero crossing date
Airborne observation	North	274 ± 44.4	207 ± 34.8	66 ± 10.4	140 ± 10.9
	South	408 ± 41.2	66 ± 21.4	270 ± 8.7	349 ± 8.2

transect (Text S1 in Supporting Information S1). For error analysis, we allow these corrections for each individual inventory estimate to have uncertainty amounting to ±100% of the correction (Text S2.3 in Supporting Information S1).

We show the corrected hemispheric ΔM^{APO} for each airborne campaign in Figure 3 (points), with error bars representing 1σ uncertainty as a quadrature sum from the following sources: (a) measurement imprecision and reproducibility; (b) spread of $M_{\theta e}$ values for different reanalysis products; (c) bias correction due to limited spatial and temporal coverage of the observations; and (d) the uncertainty of the land biosphere $O_2:CO_2$ exchange ratio. To assess uncertainties in the harmonic fits, we generate an ensemble of 2000 fits. Details of the uncertainty (error bars in Figure 3) analysis are presented in Text S2 in Supporting Information S1.

### 4.2. Results and Discussion of APO Inventories

In each hemisphere, the seasonal anomaly of APO inventory generally increases in spring and summer and decreases in fall and winter (Figure 3), consistent with air-sea fluxes of O_2 driving the seasonal cycle of atmospheric APO. In the Southern Hemisphere, the austral spring/summer rise is more rapid than the austral fall/winter decrease by ∼1.5 months. In the Northern Hemisphere, due to a broad summer peak, the rising period is ∼3 months shorter than that in the Southern Hemisphere.

Figure 3 and Table 1 show that the seasonal amplitude of atmospheric APO inventory in the Southern Hemisphere (408 ± 41.2 Tmol) is significantly larger than in the Northern Hemisphere (274 ± 44.4 Tmol). The cycle in the Southern Hemisphere is heavily dominated by the first harmonic, and the phase indicated by the upward zero-crossing is 4 weeks later relative to the cycle in the Northern Hemisphere when measured relative to the hemispheric solstice date.

The period of seasonal maximum APO inventory is broader in the Northern Hemisphere than in the Southern Hemisphere. Similar broad maxima are seen at northern land stations (e.g., Hateruma Island at 24.1°N, Barrow at 71.3°N, and Alert at 82.5°N) and in the subtropical (20–40°N) Northwest Pacific, as shown by shipborne measurements (Nevison et al., 2015; Tohjima et al., 2012, 2019).

The annual average APO is lower in the Northern Hemisphere by 6.4 ± 1.11 per meg (93.3 ± 16.21 Tmol) relative to the Southern Hemisphere, based on the annual mean from the 2-harmonic fits. In comparison, Resplandy et al. (2016) reported a northern APO deficit of 10.4 ± 0.9 per meg using HIPPO data in the mid-troposphere between 40°N and 60°N, which they use to constrain the interhemispheric ocean heat flux, based on the close connection between APO and heat fluxes. These two estimates are not directly comparable because our estimate includes data from lower latitudes, where we expect a smaller APO gradient between the two hemispheres (Resplandy et al., 2016).

Each APO seasonal inventory estimate has uncertainty up to ±72 Tmol (Error bars in Figure 3, details in Table S4 and S5 in Supporting Information S1). Of the several contributions to the uncertainty, the dominant contribution is measurement imprecision and reproducibility, which is mainly limited by campaign-to-campaign calibration or sampling offsets. The corrections for limited coverage and the uncertainty for corrections are small because we have sufficient observations across $M_{\theta e}$ (or on θ_e) surfaces in the hemisphere and because the along-$M_{\theta e}$ APO gradients are uniformly small (Figure 2a) in both high and low $M_{\theta e}$ bins. For the low $M_{\theta e}$ bins, the small gradient is due to rapid adiabatic APO mixing along $M_{\theta e}$. For the high $M_{\theta e}$ bins, the small gradient can be partially attributed to the small magnitude of surface APO flux due to weak seasonal forcing.
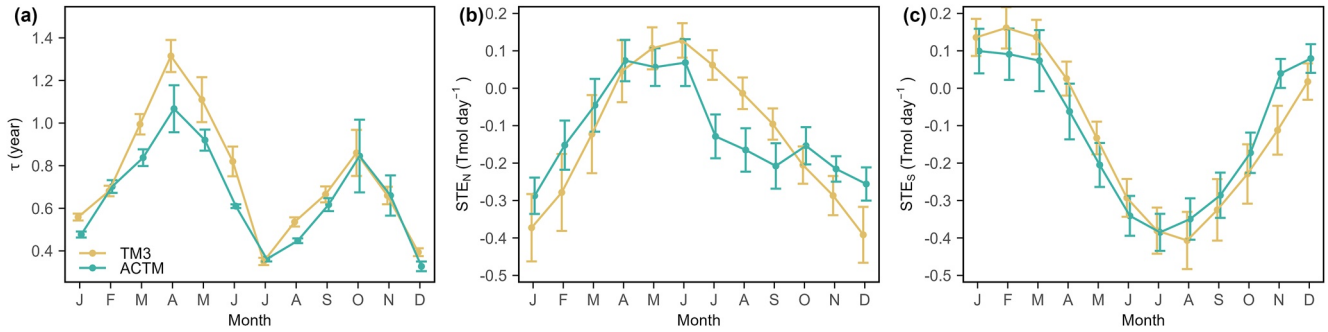
Figure 4. (a) Climatological monthly seasonal APO exchange time scale (τ) between the Northern and the Southern tropospheres. (b and c) Troposphere-stratosphere APO exchange rates (Tmol day^{-1}) in the Northern Hemisphere (STE$_N$) and Southern Hemisphere (STE$_S$), respectively. Positive value denotes troposphere to stratosphere APO transport. τ, STE$_N$, and STE$_S$ are computed using air-sea APO flux from Jena CarboScope APO inversion and tropospheric APO inventory from Jena-TM3 and Jena-ACTM (model descriptions see Section 2.5). The 1σ uncertainty is computed as the standard deviation of τ for each corresponding month from 2009 to 2018. Methods are presented in Appendix A.

5. Seasonal Cycles of Hemispheric Air-Sea APO Fluxes

5.1. Method

We calculate total area-integrated APO fluxes (including all sources of exchange, i.e., from the ocean and fossil fuel emission) in the Northern Hemisphere (F_N^{APO}) and Southern Hemisphere (F_S^{APO}) (Tmol day^{-1}) from airborne observations, using a two-box model:

$$F_N^{\mathrm{APO}}(t) = \frac{\partial M_N^{\mathrm{APO}}(t)}{\partial t} + L_N(t) \tag{15}$$

$$F_S^{\mathrm{APO}}(t) = \frac{\partial M_S^{\mathrm{APO}}(t)}{\partial t} + L_S(t) \tag{16}$$

where $\frac{\partial M_N^{\mathrm{APO}}(t)}{\partial t}$ and $\frac{\partial M_S^{\mathrm{APO}}(t)}{\partial t}$ are the tropospheric APO inventory changes (Tmol day^{-1}) of each hemisphere and $L_N(t)$ and $L_S(t)$ are "leakage" terms across the Equator and tropopause. Here, we calculate daily APO inventory changes in each hemisphere by combining the 2-harmonic fitted seasonal APO inventories from Section 4 with the previously removed annual average hemispheric APO and the removed long-term APO trend. Combining these components allows us to resolve both seasonal and annual mean components of the flux. We base the trend on observations from surface stations (Section 2.3), scaled to yield hemispheric inventories (Equation 14). We use the same global trend for both hemispheres.

The leakage terms are included in Equations 17 and 18 to account for the transport of ΔAPO between hemispheres, and between the troposphere and the stratosphere. Positive leakage represents the transport out of the troposphere in each hemisphere. We parameterize the leakage according to:

$$L_N(t) = \frac{\left(M_N^{\mathrm{APO}}(t) - M_S^{\mathrm{APO}}(t)\right)}{\tau(t)} + \mathrm{STE}_N \tag{17}$$

$$L_S(t) = -\frac{\left(M_N^{\mathrm{APO}}(t) - M_S^{\mathrm{APO}}(t)\right)}{\tau(t)} + \mathrm{STE}_S \tag{18}$$

where $\tau(t)$ is a climatological inter-hemisphere APO exchange time scale with a unit of year, and STE$_N(t)$ and STE$_S(t)$ are climatological stratosphere-troposphere exchange rate (Tmol day^{-1}). We estimate $\tau(t)$, STE$_N(t)$, and STE$_N$(t) using two transport models (TM3 and MIROC-ACTM) as described in Appendix A. We show climatological monthly $\tau(t)$, STE$_N(t)$, and STE$_N$(t) in Figure 4 along with the interannual variability from 2009 to 2018 (shown as $\pm 1\sigma$). To yield daily values of τ, STE$_S$, and STE$_N$ for application in Equations 15 and 16, we fit the climatological monthly results to a two-harmonic fit (Figure 4).

We validate the two-box model by successfully reconstructing the daily Jena inversion APO flux using troposphere APO inventories and parameters $\tau(t)$, STE_N, and STE_S from two transport models (TM3 and ACTM), as shown in Figure S5 in Supporting Information S1. This reconstruction shows small RMSE up to 0.53 Tmol day^{-1}. Seasonal cycle of air-sea APO flux is dominated by the inventory term ($\frac{dM^{APO}}{dt}$), with relatively small contribution form the leakage term. The leakage term causes the flux amplitude to be larger than the inventory amplitude by 22.1% in the Northern Hemisphere and 23.2% in the Southern Hemisphere, as shown in Figure S6 in Supporting Information S1.

The area-integrated APO fluxes calculated using Equations 15 and 16 include small contributions from APO fluxes directly caused by the burning of fossil-fuel ($F^{APO(ff)}$). To resolve APO fluxes due to ocean fluxes alone, we compute residual fluxes according to

$$
\begin{aligned}
F^{APO(ocn)} &= F^{APO} - F^{APO(ff)} \\
&= F^{APO} - \left(F^{O_2(ff)} + 1.1 F^{CO_2(ff)} \right)
\end{aligned}
\tag{19}
$$

where fossil fuel O_2 flux is calculated by scaling corresponding CO_2 flux

$$
F^{O_2(ff)} = -1.35 F^{CO_2(ff)}
\tag{20}
$$

The factor of -1.35 is supported by emission ratios from Keeling et al. (1998) and emissions by fuel type from the Global Carbon Budget (Friedlingstein et al., 2022). We use $F^{CO_2(ff)}$ averaged from Open-source Data Inventory for Anthropogenic CO_2 (ODIAC, Oda et al., 2018) and GCP-GridFEDv2022.2 (Jones et al., 2021) (for details see Text S3.2 in Supporting Information S1). The fossil fuel emission contributes significantly to the loss of APO in the Northern Hemisphere, amounting to an annual uptake of 208.5 Tmol, but its impact on the seasonal cycle is small, accounting for 1.2% of the air-sea flux seasonal amplitude (Figure S6 in Supporting Information S1). In the Southern Hemisphere, the annual APO uptake of fossil fuels is small, amounting to 15.7 Tmol and 0.06% of the air-sea flux seasonal amplitude (Figure S6 in Supporting Information S1).

We show the seasonal cycle of air-sea APO flux of each hemisphere in Figure 5, calculated by applying the 2-harmonic seasonal APO inventory anomalies in each hemisphere that are resolved in Section 4 to the 2-box model and correcting for the fossil fuel component. The flux uncertainties are calculated from an ensemble of model runs that uses 2000 iterations of harmonic fits from the previous section and convolving these with additional uncertainties in the box-model transport parameter and fossil fuel correction (Text S3 in Supporting Information S1). Related statistics (maximum and minimum fluxes, maximum and minimum date, APO seasonal net outgassing (SNO), upward zero-crossing date, and annual flux) are summarized in Table 2. SNO is defined as the area under the positive portion of the 2-harmonic fitted seasonal cycle curve after removing the annual mean flux, which is a measure of the contribution of air-sea APO flux to the seasonal cycle of atmospheric APO (Garcia & Keeling, 2001). The annual mean flux is calculated as the integration of daily flux over the course of the seasonal cycle.

5.2. Results and Discussion of Air-Sea APO Fluxes

We found significantly larger SNO in the Southern Hemisphere (518 ± 52.6 Tmol) than in the Northern Hemisphere (342 ± 52.1 Tmol). Dividing SNO by the ocean area in each hemisphere, we find a flux per unit area that is also larger (within 1σ uncertainty) in the south (2.49 ± 0.253 mol m^{-2}) than in the north (2.21 ± 0.337 mol m^{-2}).

In both hemispheres (Figures 5a and 5b), the APO flux cycle is non sinusoidal, with the rise occurring more rapidly than the decline. Compared to the hemispheric solstice date, the timing of this rise, based on the upward zero-crossing, is earlier by 3 weeks in the Northern Hemisphere (late March) compared to the Southern Hemisphere (mid-October) (Figures 5c and Table 2). Similarly, the date of maximum summer outgassing is earlier by 5 weeks in the Northern Hemisphere. These estimated phase asymmetries are not very sensitive to assumptions about interhemispheric APO leakage (Figure S6 in Supporting Information S1).

Differences are also notable in the shape of the declining portion of the cycle. The Southern Hemisphere decrease is relatively steady, while the Northern Hemisphere decrease starts with a slow drop from May to August followed by a late summer plateau till October, and then a rapid drop through January. This near zero flux during the summer plateau leads to a broad atmospheric APO peak in the Northern Hemisphere (Figure 3a), corresponding
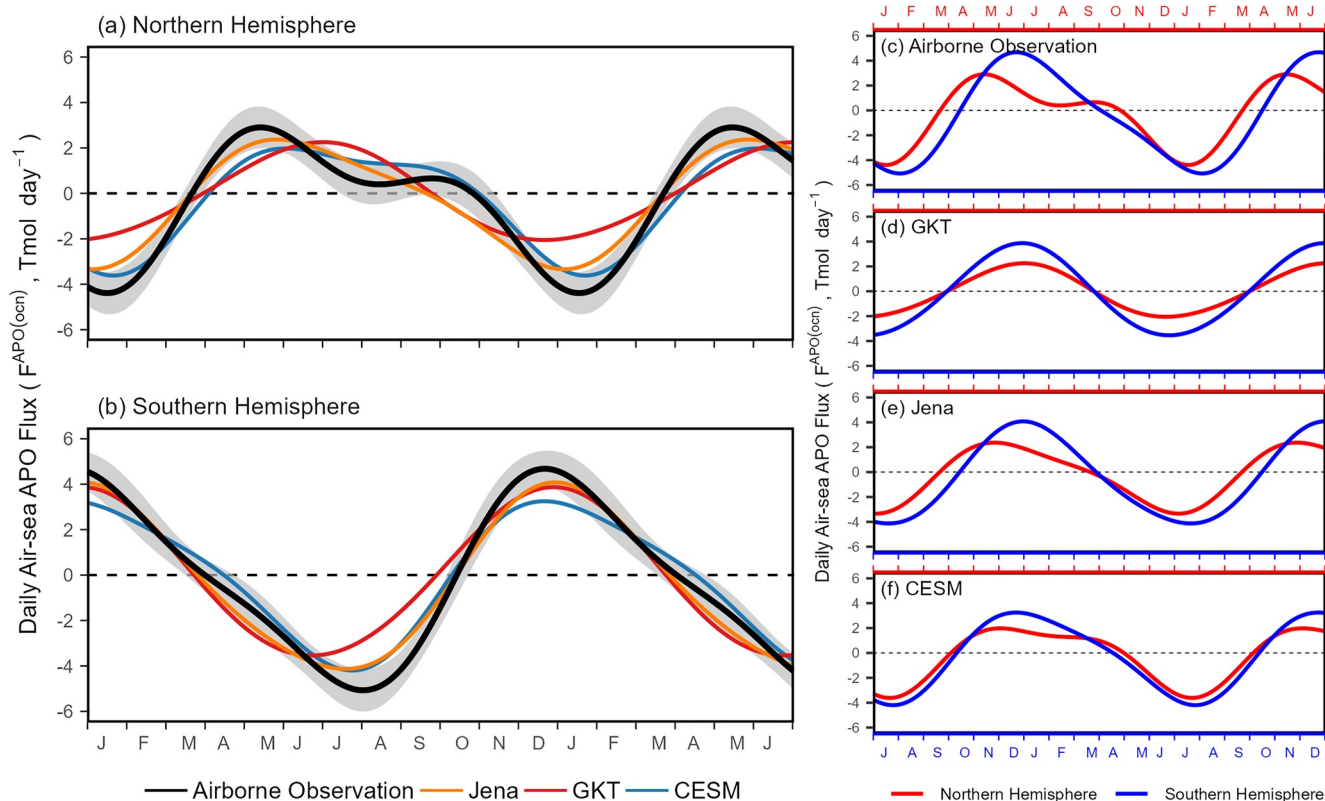
Figure 5. Seasonality of area-integrated daily air-sea APO fluxes in the Northern (a) and Southern (b) Hemispheres. We show our estimate of the flux cycle as black curves. The 1σ uncertainty (gray shading) is calculated as the standard deviation of 2000 iteration of 2-harmonic fit to flux estimates (for details see Text S3 in Supporting Information S1). For comparison, we also show the modeled daily air-sea APO fluxes from Jena (orange), GKT (red), and Community Earth System Model (blue). The first half-year is repeated. (c–f) Comparing the seasonal cycle of APO fluxes from airborne observations and other products in the Northern and Southern Hemisphere, with the cycle in the Southern Hemisphere shifted by 6 months (starting from July, see blue ticks on the bottom). The first half year is repeated. We note that only GKT is adjusted to have zero annual flux.

to a period of longer (but weaker) APO outgassing in the Northern Hemisphere (Figure 5c). A similar summer plateau is clearly manifested in the CESM but is weak in the Jena inversion. This feature, however, is not observed in GKT (Figure 5d).

Could the phase asymmetry in the APO cycles between the hemispheres be caused by differences in the phasing of seasonal ocean warming and cooling? The simulated flux cycle from GKT, which is calculated by assuming air-sea O_2 flux is in phase with ocean heat flux, does not support this hypothesis because it does not show such phase asymmetry between hemispheres (Figure 5d).

The phase asymmetry is likely caused by other physical and biogeochemical processes that drive the surface ocean O_2 change. A significant factor may be differences in the timing of the spring bloom between hemispheres. Satellite-based chlorophyll concentrations suggest that the spring bloom is roughly one month earlier in the Northern Hemisphere compared to the Southern Hemisphere, with the bloom peaking in April and May over the mid-latitudes (30–50°N) of the North Atlantic and Pacific and peaking in November to January at mid-latitudes (30–50°S) of the Southern Hemisphere (Sapiano et al., 2012). The earlier spring-time O_2 outgassing in the Northern Hemisphere may also be influenced by differences in O_2 equilibration time scale in the mixed layer. As shown in de Boyer Montégut et al. (2004), the mixed layer depth in the mid-latitude Northern Hemisphere is between 10 and 100 m in spring (April), whereas the depth in the mid-latitude Southern Hemisphere is generally between 100 and 300 m in spring (October). Assuming a gas exchange velocity of 3 m day^{-1} and a difference in mixed layer depth of 100 m, the equilibration time in the Northern Hemisphere would be about 1 month faster than that in the Southern Hemisphere.

The asymmetry in the breadth of the late summer and fall outgassing period (broader and stronger in the Northern Hemisphere) may be influenced by the presence of the shallow oxygen maximum (SOM) in the North Pacific (Hayward, 1994; Shulenberger & Reid, 1981), as noted by Ishidoya et al. (2016). The SOM is generated by the strong surface ocean stratification in the summer, which traps photosynthetically produced O_2 below the mixed layer, delaying O_2 outgassing until the fall, when the mixed layer deepens. The SOM is confirmed by Argo float measurements over the western subtropical North Pacific (17.7–20.2°N and 162–164.5°E), which show clear oxygen supersaturation beneath the mixed layer from May to November (Yang et al., 2017). We also find, in the CESM configuration, an oxygen supersaturation zone at around 40–60 m deep over the mid-latitude (20–45°N) of the Northern Pacific from July to October (not shown), suggesting that the summer-to-fall plateau in CESM is SOM-related. We could not find a similarly strong late summer and fall plateau in the Southern Hemisphere in both airborne-based flux estimates and the CESM, consistent with the summer mixed layer being deeper in the Southern Hemisphere (Kara et al., 2003).

The phase and SNO differences between hemispheres may also have contributed from tropical ocean fluxes. The CESM and the Jena inversion suggest clear seasonal fluxes in the 20°S–20°N band (Figure S7 in Supporting Information S1). The APO fluxes integrated over this band have similar phasing to fluxes in the extratropical Southern Hemisphere, with ocean APO uptake during the austral winter and outgassing during the austral summer. These tropical fluxes therefore contribute to a larger SNO in the Southern Hemisphere and smaller SNO in the Northern Hemisphere, while also contributing to earlier phasing in the north (Figure S7 in Supporting Information S1).

Table 2 also provides annual APO fluxes, based on the secular components of the box model, yielding net global ocean APO uptake of 207 Tmol. The gain of APO in the global ocean is expected from the ocean uptake of anthropogenic CO_2, with small impact from a climate driven net outgassing of APO due to ocean heat uptake from the atmosphere (32 ± 19.6 Tmol net releasing per year) and aerosol-related APO outgassing due to ocean fertilization driven by atmospheric deposition of anthropogenic aerosol (8 ± 4.1 Tmol net releasing per year) (Resplandy et al., 2019). Here we estimate an annual ocean anthropogenic CO_2 uptake of 2.7 ± 0.25 PgC (converted from 247 ± 22.8 Tmol of APO) by subtracting the global climate-driven APO impact and aerosol-related impact from our global annual oceanic APO uptake estimates (for method see Text S4 in Supporting Information S1). Our estimation is close to the value (2.8 ± 0.4 PgC) reported in the Global Carbon Budget 2021 during the decade 2011–2020 (Friedlingstein et al., 2022).

The hemispheric flux estimates are transport model-dependent because we use TM3 and ACTM models to correct for sparse spatial and temporal sampling and to derive leakage terms in the box model. This impact is small because the flux cycles are dominated by the atmospheric inventory change on the hemispheric scale (Figure S6 in Supporting Information S1). Using the TM3 model alone or ACTM alone only leads to a small SNO difference of 14 Tmol (4.1%) and 17 Tmol (3.3%) in the Northern and Southern Hemisphere, respectively (larger if using ACTM).

Can the airborne data resolve changes in the seasonal cycles over time? Comparing the SNO estimated using HIPPO (2009–2011) data alone or ATom (2016–2018) data alone (by harmonic fits to subsets of the transects), we find SNO of ATom is 5% and 2% larger than that of HIPPO in the Northern and Southern Hemisphere respectively. These changes are not significant compared to uncertainties.

6. Comparisons to Other APO Flux Estimates

6.1. Comparison to GKT

We found systematic differences in seasonal amplitudes and phases between our airborne observation-based estimates and the GKT climatology (Figure 5). The comparison suggests that there are significant limitations to GKT fluxes at the mid- to high-latitudes of the Northern Hemisphere, based on discrepancies in the seasonal phases of APO inventory cycle in the mid- to high $M_{\theta e}$ bins (Figure S2 in Supporting Information S1). The O_2 fluxes from the GKT climatology used dissolved O_{228} data with large gaps in spatial and temporal coverage, especially over the high latitudes (Najjar & Keeling, 1997). To interpolate these sparse data, Garcia and Keeling (2001) assumed that O_2 fluxes are exactly in phase with ocean heat fluxes at a constant ratio over large latitude bands, an approach which has known limitations (Bent, 2014; Sun et al., 2017). These limitations in the coverage of samplings and assumptions lead to a significant underestimate of the northern

Table 2
Statistical Indices of the Seasonal Cycle of Air-Sea APO Fluxes From Two-Harmonic Fits for Each Hemisphere Computed From Airborne Observations, Jena Inversion, GKT, and Community Earth System Model

Product	Hem.	Max. fluxes (Tmol day^{-1})	Max. date	Min. fluxes (Tmol day^{-1})	Min. date	SNO (Tmol)	Upward zero-crossing date	Annual flux (Tmol)
Airborne observation	North	2.9 ± 0.83	135 ± 25.3	-4.4 ± 0.88	16 ± 11.9	342 ± 52.1	79 ± 14.4	-111 ± 34.7
	South	4.7 ± 0.79	354 ± 14.1	-5.1 ± 0.86	214 ± 15.9	518 ± 52.6	284 ± 7.8	-96 ± 34.6
Jena inversion	North	2.4	147	-3.3	5	311	77	-101
	South	4.1	363	-4.1	200	471	283	-113
GKT	North	2.3	183	-2.1	354	250	90	/
	South	3.9	362	-3.5	174	430	271	/
CESM	North	2.0	154	-3.6	21	312	92	-71
	South	3.2	354	-4.2	206	415	281	-66

Note. We note that seasonal net outgassing (SNO) and upward zero-crossing date is calculated based on the flux cycles with annual mean flux removed.

winter-time O_2 uptake (Figure 5a). We find that, in the Labrador Sea, the Garcia and Keeling (2001) climatology yields a winter-time (October to March) O_2 uptake of 9.1 mol m^{-2}, compared to more recent estimates of 22.1 ± 2.5 mol m^{-2} for 2016 (Atamanchuk et al., 2020) and 29.1 ± 3.8 mol m^{-2} for 2015 (Koelling et al., 2017).

6.2. Comparison to Jena APO Inversion

We find relatively good agreement between our hemispheric flux estimates and from the Jena inversions (Figure 5 and Table 2). The most obvious differences in the Northern Hemisphere are the too weak northern summer plateau and too small northern winter-time oceanic APO uptake. The too small winter-time uptake in inversion estimates based on surface data relative to airborne-based estimates is also found in Resplandy et al. (2016), and is attributed to an underestimation of the vertical mixing by the atmospheric transport models over the north Atlantic. In the Southern Hemisphere, we find evident differences in atmospheric APO seasonal cycles in individual $M_{\theta e}$ bins, where the Jena-TM3 shows a smaller change in APO amplitude from low to high $M_{\theta e}$ than the observations (Figure S2 in Supporting Information S1). This discrepancy may point to the TM3 model overestimating mixing (across $M_{\theta e}$) in the Southern Hemisphere. This interpretation is also supported by a comparison (not shown) between the Jena inversion and shipboard measurements over the Western Pacific from 5°S to 24°S from Tohjima et al. (2012), where the Jena inversion yields amplitudes that are too large by up to 40%.

6.3. Comparison to CESM

In the Northern Hemisphere, the CESM shows a too weak spring (MAM) APO outgassing of ~1.5 Tmol day^{-1} but too large fall (SON) outgassing of ~1.2 Tmol day^{-1} (Figure 5a). These discrepancies may result from limitations in the combination of modeled spring-summer export production and fall-time ventilation, as seen in an earlier version of CESM (Nevison et al., 2015). Nevison et al. (2015) pointed out that fall deep water ventilation in multiple Earth System Models is too weak, which reduces the transport of O_2-depleted deep water into the surface ocean during the northern fall.

In the Southern Hemisphere, the seasonal phases of the CESM are close to airborne observations, but peak-to-peak amplitude and SNO are lower than the airborne results.

7. Summary and Outlook

We use APO observations from two recent airborne projects, HIPPO and ATom, to resolve climatological seasonal APO tropospheric distributions (Section 3), tropospheric inventories (Section 4), and air-sea fluxes (Section 5) at the hemispheric scale. Airborne observations are organized on a mass-weighted moist isentropic coordinate ($M_{\theta e}$) as an alternative to latitude to analyze atmospheric distributions and compute tropospheric inventories.

The airborne data resolve clear seasonal APO changes within and between hemispheres (Figure 2). The seasonal amplitude is larger in the Southern Hemisphere and is larger in the high-latitudes (low $M_{\theta e}$) of each hemisphere. The seasonal phase also shows a clear gradient over latitudes ($M_{\theta e}$). In the Northern Hemisphere, we find an earlier phase in the lowest latitude (highest $M_{\theta e}$), whereas in the Southern Hemisphere, we find an earlier phase in the high latitude (lowest $M_{\theta e}$). These different patterns are also observed at surface stations and shipboard measurements over the Pacific Ocean (Keeling et al., 1998; Tohjima et al., 2012).

We also compute hemispheric-scale air-sea fluxes from hemispheric inventories using a 2-box model (Appendix A) that accounts for the surface APO flux, the inter-hemispheric APO exchange, and the troposphere-stratosphere APO exchange. We compare our box-model inverted flux to other model- and observation-based products, such as the Jena APO inversion (updates of Rödenbeck et al., 2008), the Garcia and Keeling (2001) O_2 flux climatology, and one configuration of CESM, to identify limitations in these products (Section 6).

Our estimates of air-sea APO fluxes (Figure 5) show clear seasonal cycles in both hemispheres, with the ocean releasing APO in the spring and summer and taking up APO in the fall and winter. The cycle in the Northern Hemisphere has a smaller seasonal amplitude, an earlier (relative to the hemispheric solstice date), and a longer period of net outgassing (Figure 5) compared to the cycle in the Southern Hemisphere, suggesting differences

between the hemispheres in physical and biogeochemical mechanisms, such as a strong subsurface oxygen maximum (SOM) and faster mixed layer equilibration time scale in the Northern Hemisphere.

Our results point to two important flux features in the Northern Hemisphere. The first feature is a strong oceanic O_2 uptake in January. This strong uptake feature is clearly underestimated in observation-based products (i.e., GKT). We attribute the bias in GKT to limited coverage of dissolved O_2 measurements over northern high latitudes and the assumption that O_2 fluxes are exactly in phase with ocean heat fluxes at a constant ratio over large latitude bands, which fails to account for processes during winter-time deep convection events.

The second feature is a period of weak APO outgassing in the northern late summer and fall. This signal is likely related to the development of the SOM, which stores spring-time photosynthetically produced O_2 below the mixed layer, and delays the O_2 outgassing until the fall, when the mixed layer deepens. In comparison with airborne-based estimates during the northern late summer and fall, the CESM shows too strong APO outgassing. On the other hand, two observation-based products (GKT and the Jena inversion) do not capture this northern APO outgassing during the late summer and fall.

Given the obvious limitations of the Garcia and Keeling (2001) O_2 flux climatology, our study motivates the creation of improved climatology, taking advantage of expanded measurements of O_2 with atmospheric calibration on biogeochemical Argo floats (Bittig & Körtzinger, 2015, 2017; Bushinsky et al., 2016, 2017; Claustre et al., 2020; Johnson et al., 2015). Our study also motivates future work focusing on regions with winter-time deep convection (e.g., Labrador Sea and western boundary currents) and summer-time stratification (e.g., northwest Pacific) from both modeling and observational perspectives. More realistic depictions of ocean ventilation in general circulation models (e.g., CESM) are needed, along with improved coverage in atmospheric APO station measurements that better target convective regions along with improved skill of modeled atmospheric transport over these regions. Finally, a regular program of hemispheric to global scale airborne transects, such as HIPPO and ATom but at higher frequency, would greatly improve our ability to constrain APO fluxes and resolve interannual variations and trends tied to climate and biogeochemical forcing.

Appendix A: Box Model

We use a box model (Figure A1) as a modified version of the two-box model in Lintner et al. (2004) and Patra et al. (2009) to quantify the hemispheric APO leakage. The model follows:

$$L_N(t) = F_N^{\text{APO}}(t) - \frac{\partial M_N^{\text{APO}}(t)}{\partial t} = \frac{\left(M_N^{\text{APO}}(t) - M_S^{\text{APO}}(t)\right)}{\tau(t)} + \text{STE}_N(t) \tag{A1}$$
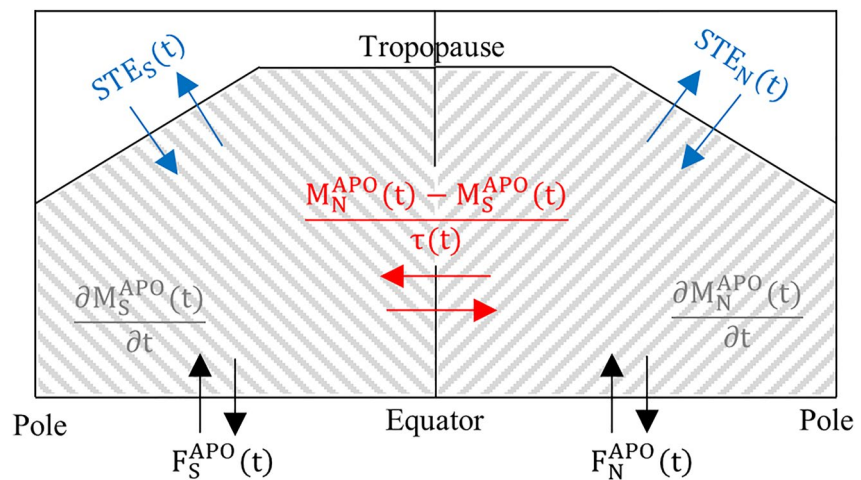
Figure A1. Schematic of the box model.

$$L_S(t) = F_S^{\text{APO}}(t) - \frac{\partial M_S^{\text{APO}}(t)}{\partial t} = -\frac{\left(M_N^{\text{APO}}(t) - M_S^{\text{APO}}(t)\right)}{\tau(t)} + \text{STE}_S(t) \tag{A2}$$

with climatological monthly $\tau(t)$ as the inter-hemisphere APO exchange time with unit of year, and monthly STE_N and STE_S as the stratosphere-troposphere APO exchange with unit of Tmol day^{-1}.

STE_N and STE_S are directly calculated from daily Jena-TM3 and Jena-ACTM as the time derivative of stratosphere APO inventory of each hemisphere, assuming interhemispheric APO exchange in the stratosphere is negligible compared to the exchange across tropopause (Butchart, 2014; Stohl et al., 2003), following:

$$\text{STE}_N(t) = \frac{\partial M_N^{\text{APO(Strat)}}(t)}{\partial t} \tag{A3}$$

$$\text{STE}_S(t) = \frac{\partial M_S^{\text{APO(Strat)}}(t)}{\partial t} \tag{A4}$$

where $M_N^{\text{APO(Strat)}}(t)$ and $M_S^{\text{APO(Strat)}}(t)$ are the stratosphere APO inventory in the Northern and Southern Hemisphere, respectively. We report climatological monthly STE in Figures 4b and 4c, with the 1σ uncertainty showing interannual variability.

We solve for the parameter $\tau(t)$ according to:

$$\tau(t) = \frac{2\left(M_N^{\text{APO}}(t) - M_S^{\text{APO}}(t)\right)}{F_N^{\text{APO}}(t) - F_S^{\text{APO}}(t) - \frac{\partial\left(M_N^{\text{APO}}(t) - M_S^{\text{APO}}(t)\right)}{\partial t} - \text{STE}_N(t) + \text{STE}_S(t)} \tag{A5}$$

We use monthly $F_N^{\text{APO}}(t)$ and $F_S^{\text{APO}}(t)$ averaged from daily Jena inversion APO flux, and monthly $M_N^{\text{APO}}(t)$ and $M_S^{\text{APO}}(t)$ averaged from daily Jena-TM3 or Jena-ACTM, to compute the climatological monthly $\tau(t)$ (averaged for each month from 2009 to 2018). We report $\tau(t)$ of each model in Figure 4a, with the 1σ uncertainty showing interannual variability. In Figure 4a, we show that both the TM3 and ACTM transport models suggest a faster inter-hemisphere mixing in summer and winter, and a slower mixing in spring and fall.

To examine the skill of the box model in producing daily air-sea APO fluxes, we compare simulated APO fluxes (Jena inversion) with reconstructed APO fluxes calculated using simulated APO inventories based on the Jena inversion APO flux forward transported by the TM3 model (Jena-TM3), and the ACTM model (Jena-ACTM), together with corresponding climatological TM3-based or ACTM-based τ and STE (Figure S5 in Supporting Information S1). The daily τ and STE is computed by a 2-harmonic fit to climatological monthly τ and climatological monthly STE. We show (Figure S5 in Supporting Information S1) that this box model can reconstruct the hemispheric air-sea APO flux reasonably well, with an RMSE of daily flux smaller than 0.53 Tmol day^{-1}. This method does not bias the SNO results, as we find a small difference of averaged SNO (2009–2018) between the reconstructed APO flux and the original APO flux of 18 Tmol (5.8%) in the Northern Hemisphere and 32 Tmol (6.3%) in the Southern Hemisphere.

Data Availability Statement

All ancillary HIPPO 10 s merge data are available from https://doi.org/10.3334/CDIAC/HIPPO_010 (Wofsy et al., 2017). We use updated HIPPO AO2 data from https://doi.org/10.5065/D6J38QVV (Stephens et al., 2021a), https://doi.org/10.5065/D65Q4TF0 (Stephens et al., 2021b), https://doi.org/10.5065/D67H1GXJ (Stephens et al., 2021c), https://doi.org/10.5065/D679431D (Stephens et al., 2021d), and https://doi.org/10.5065/D6WW7G0D (Stephens et al., 2021e). All ATom 10s merge data are available from https://doi.org/10.3334/ORNLDAAC/1925 (Wofsy et al., 2021). Jena CarboScope APO inversion (version: apo99XS_v2022) is available from https://www.bgc-jena.mpg.de/CarboScope/?ID=apo99XS_v2022 (Rödenbeck et al., 2008). Garcia and Keeling (2001a, 2001b) climatological monthly O2 flux data and climatological monthly N2 flux data from ECCO version 4 are available from https://doi.org/10.5281/zenodo.6516046 (Jin, 2022). The CESM air-sea APO flux fields are available upon request. The atmospheric field of APO forward transported by TM3 and ACTM model are available upon request. $\theta_e-M_{\theta_e}$ look-up tables with daily resolution and 1 K intervals in θ_e from 1980 to 2018 computed from ERA-Interim are available at https://doi.org/10.5281/zenodo.4420398 (Jin, 2021).

References

Atamanchuk, D., Koelling, J., Send, U., & Wallace, D. W. R. (2020). Rapid transfer of oxygen to the deep ocean mediated by bubbles. *Nature Geoscience*, *13*(3), 232–237. https://doi.org/10.1038/s41561-020-0532-2

Battle, M., Fletcher, S. M., Bender, M. L., Keeling, R. F., Manning, A. C., Gruber, N., et al. (2006). Atmospheric potential oxygen: New observations and their implications for some atmospheric and oceanic models. *Global Biogeochemical Cycles*, *20*(1), GB1010. https://doi.org/10.1029/2005GB002534

Bent, J. D. (2014). *Airborne oxygen measurements over the Southern Ocean as an integrated constraint of seasonal biogeochemical processes*. University of California.

Bittig, H. C., & Körtzinger, A. (2015). Tackling oxygen optode drift: Near-surface and in-air oxygen optode measurements on a float provide an accurate in situ reference. *Journal of Atmospheric and Oceanic Technology*, *32*(8), 1536–1543. https://doi.org/10.1175/JTECH-D-14-00162.1

Bittig, H. C., & Körtzinger, A. (2017). Technical note: Update on response times, in-air measurements, and in situ drift for oxygen optodes on profiling platforms. *Ocean Science*, *13*(1), 1–11. https://doi.org/10.5194/os-13-1-2017

Bushinsky, S. M., Emerson, S. R., Riser, S. C., & Swift, D. D. (2016). Accurate oxygen measurements on modified Argo floats using in situ air calibrations. *Limnology and Oceanography: Methods*, *14*(8), 491–505. https://doi.org/10.1002/lom3.10107

Bushinsky, S. M., Gray, A. R., Johnson, K. S., & Sarmiento, J. L. (2017). Oxygen in the southern ocean from Argo floats: Determination of processes driving air-sea fluxes. *Journal of Geophysical Research: Oceans*, *122*(11), 8661–8682. https://doi.org/10.1002/2017JC012923

Butchart, N. (2014). The Brewer-Dobson circulation. *Reviews of Geophysics*, *52*(2), 157–184. https://doi.org/10.1002/2013RG000448

Claustre, H., Johnson, K. S., & Takeshita, Y. (2020). Observing the global ocean with biogeochemical-Argo. *Annual Review of Marine Science*, *12*(1), 23–48. https://doi.org/10.1146/annurev-marine-010419-010956

Dee, D. P., Uppala, S. M., Simmons, A. J., Berrisford, P., Poli, P., Kobayashi, S., et al. (2011). The ERA-Interim reanalysis: Configuration and performance of the data assimilation system. *Quarterly Journal of the Royal Meteorological Society*, *137*(656), 553–597. https://doi.org/10.1002/qj.828

Dietze, H., & Oschlies, A. (2005). On the correlation between air-sea heat flux and abiotically induced oxygen gas exchange in a circulation model of the North Atlantic. *Journal of Geophysical Research C: Oceans*, *110*(C9), C09016. https://doi.org/10.1029/2004JC002453

Diskin, G. S., Podolske, J. R., Sachse, G. W., & Slate, T. A. (2002). Open-path airborne tunable diode laser hygrometer. *Diode Lasers and Applications in Atmospheric Sensing*, *4817*, 196–204. https://doi.org/10.1117/12.453736

Forget, G., Campin, J. M., Heimbach, P., Hill, C. N., Ponte, R. M., & Wunsch, C. (2015). ECCO version 4: An integrated framework for non-linear inverse modeling and global ocean state estimation. *Geoscientific Model Development*, *8*(10), 3071–3104. https://doi.org/10.5194/gmd-8-3071-2015

Friedlingstein, P., Jones, M. W., Sullivan, M. O., Andrew, R. M., Bakker, D. C. E., Hauck, J., et al. (2022). Global carbon budget 2021. *Earth System Science Data*, *14*(4), 1917–2005. https://doi.org/10.5194/essd-14-1917-2022

Gallagher, M. E., Liljestrand, F. L., Hockaday, W. C., & Masiello, C. A. (2017). Plant species, not climate, controls aboveground biomass O_2: CO_2 exchange ratios in deciduous and coniferous ecosystems. *Journal of Geophysical Research: Biogeosciences*, *122*(9), 2314–2324. https://doi.org/10.1002/2017JG003847

Garcia, & Keeling (2001a). O_2 flux (1.0). [Dataset]. Zenodo. https://doi.org/10.5281/zenodo.6516046

Garcia, E., & Keeling, F. (2001b). On the global oxygen anomaly and air-sea flux. *Journal of Geophysical Research*, *106*(C12), 31155–31166. https://doi.org/10.1029/1999JC000200

Gelaro, R., McCarty, W., Suárez, M. J., Todling, R., Molod, A., Takacs, L., et al. (2017). The modern-era retrospective analysis for research and applications, version 2 (MERRA-2). *Journal of Climate*, *30*(14), 5419–5454. https://doi.org/10.1175/JCLI-D-16-0758.1

Goto, D., Morimoto, S., Aoki, S., Patra, P. K., & Nakazawa, T. (2017). Seasonal and short-term variations in atmospheric potential oxygen at Ny-Ålesund, Svalbard. *Tellus Series B Chemical and Physical Meteorology*, *69*(1), 1311767. https://doi.org/10.1080/16000889.2017.1311767

Hamme, R. C., & Keeling, R. F. (2008). Ocean ventilation as a driver of interannual variability in atmospheric potential oxygen. *Tellus Series B Chemical and Physical Meteorology*, *60*(5), 706–717. https://doi.org/10.1111/j.1600-0889.2008.00376.x

Hayward, T. L. (1994). The shallow oxygen maximum layer and primary production. *Deep-Sea Research Part I*, *41*(3), 559–574. https://doi.org/10.1016/0967-0637(94)90095-7

Heimann, M., & Körner, S. (2003). The global atmospheric tracer model TM3: Model description and user's manual Release 3.8 a. MPI-BGC.

Hintsa, E. J., Moore, F. L., Hurst, D. F., Dutton, G. S., Hall, B. D., Nance, J. D., et al. (2021). UAS Chromatograph for Atmospheric Trace Species (UCATS)—A versatile instrument for trace gas measurements on airborne platforms. *Atmospheric Measurement Techniques*, *14*(10), 6795–6819. https://doi.org/10.5194/amt-14-6795-2021

Hockaday, W. C., Masiello, C. A., Randerson, J. T., Smernik, R. J., Baldock, J. A., Chadwick, O. A., & Harden, J. W. (2009). Measurement of soil carbon oxidation state and oxidative ratio by 13C nuclear magnetic resonance. *Journal of Geophysical Research*, *114*(2), 1–14. https://doi.org/10.1029/2008JG000803

Ishidoya, S., Tsuboi, K., Niwa, Y., Matsueda, H., Murayama, S., Ishijima, K., & Saito, K. (2022). Spatiotemporal variations of the δ(O_2/N_2), CO_2 and δ(APO) in the troposphere over the western North Pacific. *Atmospheric Chemistry and Physics*, *22*(10), 6953–6970. https://doi.org/10.5194/acp-22-6953-2022

Ishidoya, S., Uchida, H., Sasano, D., Kosugi, N., Taguchi, S., Ishii, M., et al. (2016). Ship-based observations of atmospheric potential oxygen and regional air-sea O_2 flux in the northern North Pacific and the Arctic Ocean. *Tellus Series B Chemical and Physical Meteorology*, *68*(1), 29972. https://doi.org/10.3402/tellusb.v68.29972

Jin, X., Najjar, R. G., Louanchi, F., & Doney, S. C. (2007). A modeling study of the seasonal oxygen budget of the global ocean. *Journal of Geophysical Research*, *112*(C5), C05017. https://doi.org/10.1029/2006JC003731

Jin, Y. (2021). θ-$M_{\theta e}$ lookup table (ERA-Interim) (version v1.0.0) [Dataset]. Zenodo. https://doi.org/10.5281/zenodo.4420398

Jin, Y. (2022). O_2 flux (1.0). [Dataset]. Zenodo. https://doi.org/10.5281/zenodo.6516046

Jin, Y., Keeling, R., Morgan, E., Ray, E., Parazoo, N., & Stephens, B. (2021). A mass-weighted atmospheric isentropic coordinate for mapping chemical tracers and computing inventories. *Atmospheric Chemistry and Physics*, *21*, 217–238. https://doi.org/10.5194/acp-2020-841

Johnson, K. S., Plant, J. N., Riser, S. C., & Gilbert, D. (2015). Air oxygen calibration of oxygen optodes on a profiling float array. *Journal of Atmospheric and Oceanic Technology*, *32*(11), 2160–2172. https://doi.org/10.1175/JTECH-D-15-0101.1

Jones, M. W., Andrew, R. M., Peters, G. P., Janssens-Maenhout, G., De-Gol, A. J., Ciais, P., et al. (2021). Gridded fossil CO_2 emissions and related O_2 combustion consistent with national inventories 1959–2018. *Scientific Data*, *8*(1), 1–23. https://doi.org/10.1038/s41597-020-00779-6

Kalnay, E., Kanamitsu, M., Kistler, R., Collins, W., Deaven, D., Gandin, L., et al. (1996). The NCEP/NCAR 40-year reanalysis project. *Bulletin of the American Meteorological Society*, *77*(3), 437–472. https://doi.org/10.1175/1520-0477(1996)077<0437:TNYRP>2.0.CO;2

Kara, A. B., Rochford, P. A., & Hurlburt, H. E. (2003). Mixed layer depth variability over the global ocean. *Journal of Geophysical Research C: Oceans*, *108*(C3), 3079. https://doi.org/10.1029/2000jc000736

Keeling, R., & Shertz, S. (1992). Seasonal and interannual variations in atmospheric oxygen and implications for the global carbon cycle. *Nature*, *358*(27), 723–727. https://doi.org/10.1038/358723a0

Keeling, R. F., Blaine, T., Paplawsky, B., Katz, L., Atwood, C., & Brockwell, T. (2004). Measurement of changes in atmospheric Ar/N$_2$ ratio using a rapid-switching, single-capillary mass spectrometer system. *Tellus B: Chemical and Physical Meteorology*, *56*(4), 322–338. https://doi.org/10.3402/tellusb.v56i4.16453

Keeling, R. F., Stephens, B. B., Najjar, R. G., Doney, S. C., Archer, D., & Heimann, M. (1998). Seasonal variations in the atmospheric O$_2$/N$_2$ ratio in relation to the kinetics of air-sea gas exchange. *Global Biogeochemical Cycles*, *12*(1), 141–163. https://doi.org/10.1029/97GB02339

Keeling, R. F., Walker, S. J., & Paplawsky, W. (2020). Span sensitivity of the scripps interferometric oxygen analyzer.

Kobayashi, S., Ota, Y., Harada, Y., Ebita, A., Moriya, M., Onoda, H., et al. (2015). The JRA-55 reanalysis: General specifications and basic characteristics. *Journal of the Meteorological Society of Japan*, *93*(1), 5–48. https://doi.org/10.2151/jmsj.2015-001

Koelling, J., Wallace, D. W. R., Send, U., & Karstensen, J. (2017). Intense oceanic uptake of oxygen during 2014–2015 winter convection in the Labrador Sea. *Geophysical Research Letters*, *44*(15), 7855–7864. https://doi.org/10.1002/2017GL073933

Langenfelds, R. L. (2002). *Studies of the global carbon cycle using atmospheric oxygen and associated tracers*. University of Tasmania.

Lintner, B. R., Gilliland, A. B., & Fung, I. Y. (2004). Mechanisms of convection-induced modulation of passive tracer interhemispheric transport interannual variability. *Journal of Geophysical Research: Atmospheres*, *109*, D13102. https://doi.org/10.1029/2003JD004306

Long, M. C., Moore, J. K., Lindsay, K., Levy, M., Doney, S. C., Luo, J. Y., et al. (2021). Simulations with the marine biogeochemistry library (MARBL). *Journal of Advances in Modeling Earth Systems*, *13*(12), e2021MS002647. https://doi.org/10.1029/2021MS002647

Manizza, M., Keeling, R. F., & Nevison, C. D. (2012). On the processes controlling the seasonal cycles of the air–sea fluxes of O$_2$ and N$_2$O: A modelling study. *Tellus B: Chemical and Physical Meteorology*, *64*(1), 18429. https://doi.org/10.3402/tellusb.v64i0.18429

Manning, A. C., & Keeling, R. F. (2006). Global oceanic and land biotic carbon sinks from the scripps atmospheric oxygen flask sampling network. *Tellus Series B Chemical and Physical Meteorology*, *58*(2), 95–116. https://doi.org/10.1111/j.1600-0889.2006.00175.x

Montegut, C. B., Madec, G., Fischer, A. S., Lazar, A., & Iudicone, D. (2004). Mixed layer depth over the global ocean: An examination of profile data and a profile-based climatology. *Journal of Geophysical Research*, *109*(12), 1–20. https://doi.org/10.1029/2004JC002378

Morgan, E. J., Manizza, M., Keeling, R. F., Resplandy, L., Mikaloff-Fletcher, S. E., Nevison, C. D., et al. (2021). An atmospheric constraint on the seasonal air–sea exchange of oxygen and heat in the extratropics. *Journal of Geophysical Research: Oceans*, *126*(8), e2021JC017510. https://doi.org/10.1029/2021jc017510

Naegler, T., Ciais, P., Orr, J. C., Aumont, O., & Rödenbeck, C. (2007). On evaluating ocean models with atmospheric potential oxygen. *Tellus*, *59B*(1), 138–156. https://doi.org/10.1111/j.1600-0889.2006.00197.x

Naegler, T., Ciais, P., Rodgers, K., & Levin, I. (2006). Excess radiocarbon constraints on air-sea gas exchange and the uptake of CO$_2$ by the oceans. *Geophysical Research Letters*, *33*, L11802. https://doi.org/10.1029/2005GL025408

Najjar, R. G., & Keeling, R. F. (1997). Analysis of the mean annual cycle of the dissolved oxygen anomaly in the World Ocean. *Journal of Marine Research*, *55*(1), 117–151. https://doi.org/10.1357/0022240973224481

Najjar, R. G., & Keeling, R. F. (2000). Mean annual cycle of the air-Sea oxygen flux: A global view. *Global Biogeochemical Cycles*, *14*(2), 573–584. https://doi.org/10.1029/1999GB900086

Nevison, C., Munro, D., Lovenduski, N., Cassar, N., Keeling, R., Krummel, P., & Tjiputra, J. (2018). Net community production in the southern ocean: Insights from comparing atmospheric potential oxygen to satellite ocean color algorithms and ocean models. *Geophysical Research Letters*, *45*(19), 10549–10559. https://doi.org/10.1029/2018GL079575

Nevison, C. D., Keeling, R. F., Kahru, M., Manizza, M., Mitchell, B. G., & Cassar, N. (2012). Estimating net community production in the southern ocean based on atmospheric potential oxygen and satellite ocean color data. *Global Biogeochemical Cycles*, *26*(1), GB1020. https://doi.org/10.1029/2011GB004040

Nevison, C. D., Mahowald, N. M., Doney, S. C., Lima, I. D., & Cassar, N. (2008). Impact of variable air-sea O$_2$ and CO$_2$ fluxes on atmospheric potential oxygen (APO) and land-ocean carbon sink partitioning. *Biogeosciences*, *5*(3), 875–889. https://doi.org/10.5194/bg-5-875-2008

Nevison, C. D., Manizza, M., Keeling, R. F., Kahru, M., Bopp, L., Dunne, J., et al. (2015). Evaluating the ocean biogeochemical components of Earth system models using atmospheric potential oxygen and ocean color data. *Biogeosciences*, *12*(1), 193–208. https://doi.org/10.5194/bg-12-193-2015

Nevison, C. D., Manizza, M., Keeling, R. F., Stephens, B. B., Bent, J. D., Dunne, J., et al. (2016). Evaluating CMIP5 ocean biogeochemistry and Southern Ocean carbon uptake using atmospheric potential oxygen: Present-day performance and future projection. *Geophysical Research Letters*, *43*(5), 2077–2085. https://doi.org/10.1002/2015GL067584

Oda, T., Maksyutov, S., & Andres, R. J. (2018). The open-source data inventory for anthropogenic CO$_2$, version 2016 (ODIAC2016): A global monthly fossil fuel CO$_2$ gridded emissions data product for tracer transport simulations and surface flux inversions. *Earth System Science Data*, *10*(1), 87–107. https://doi.org/10.5194/essd-10-87-2018

Parazoo, N. C., Denning, A. S., Berry, J. A., Wolf, A., Randall, D. A., Kawa, S. R., et al. (2011). Moist synoptic transport of CO$_2$ along the mid-latitude storm track. *Geophysical Research Letters*, *38*(9), L09804. https://doi.org/10.1029/2011GL047238

Patra, P. K., Takigawa, M., Dutton, G. S., Uhse, K., Ishijima, K., Lintner, B. R., et al. (2009). Transport mechanisms for synoptic, seasonal and interannual SF$_6$ variations and "age" of air in troposphere. *Atmospheric Chemistry and Physics*, *9*(4), 1209–1225. https://doi.org/10.5194/acp-9-1209-2009

Patra, P. K., Takigawa, M., Watanabe, S., Chandra, N., Ishijima, K., & Yamashita, Y. (2018). Improved chemical tracer simulation by MIROC4.0-based atmospheric chemistry-transport model (MIROC4-ACTM). *Scientific Online Letters on the Atmosphere*, *14*(0), 91–96. https://doi.org/10.2151/SOLA.2018-016

Pauluis, O., Czaja, A., & Korty, R. (2008). The global atmospheric circulation on moist isentropes. *Science*, *321*(5892), 1075–1078. https://doi.org/10.1126/science.1159649

Pickers, P. A., & Manning, A. C. (2015). Investigating bias in the application of curve fitting programs to atmospheric time series. *Atmospheric Measurement Techniques*, *8*(3), 1469–1489. https://doi.org/10.5194/amt-8-1469-2015

Pickers, P. A., Manning, A. C., Sturges, W. T., Le Quéré, C., Mikaloff Fletcher, S. E., Wilson, P. A., & Etchells, A. J. (2017). In situ measurements of atmospheric O$_2$ and CO$_2$ reveal an unexpected O$_2$ signal over the tropical Atlantic Ocean. *Global Biogeochemical Cycles*, *31*(8), 1289–1305. https://doi.org/10.1002/2017GB005631

Reinsch, C. H. (1967). Smoothing by spline functions. *Numerische Mathematik*, *10*(5), 177–183. https://doi.org/10.1007/BF02169154

Resplandy, L., Keeling, R. F., Eddebbar, Y., Brooks, M., Wang, R., Bopp, L., et al. (2019). Quantification of ocean heat uptake from changes in atmospheric O$_2$ and CO$_2$ composition. *Scientific Reports*, *9*(1), 1–10. https://doi.org/10.1038/s41598-019-56490-z

Resplandy, L., Keeling, R. F., Stephens, B. B., Bent, J. D., Jacobson, A., Rödenbeck, C., & Khatiwala, S. (2016). Constraints on oceanic meridional heat transport from combined measurements of oxygen and carbon. *Climate Dynamics*, *47*(9–10), 3335–3357. https://doi.org/10.1007/s00382-016-3029-3

Rödenbeck, C., Le Quéré, C., Heimann, M., & Keeling, R. F. (2008). Interannual variability in oceanic biogeochemical processes inferred by inversion of atmospheric O_2/N_2 and CO_2 data. *Tellus B: Chemical and Physical Meteorology*, *60*(5), 685–705. https://doi.org/10.1111/j.1600-0889.2008.00375.x

Santoni, G. W., Daube, B. C., Kort, E. A., Jiménez, R., Park, S., Pittman, J. V., et al. (2014). Evaluation of the airborne quantum cascade laser spectrometer (QCLS) measurements of the carbon and greenhouse gas suite - CO_2, CH_4, N_2O, and CO—During the CalNex and HIPPO Campaigns. *Atmospheric Measurement Techniques*, *7*(6), 1509–1526. https://doi.org/10.5194/amt-7-1509-2014

Sapiano, M. R. P., Brown, C. W., Schollaert Uz, S., & Vargas, M. (2012). Establishing a global climatology of marine phytoplankton phenological characteristics. *Journal of Geophysical Research*, *117*(8), 1–16. https://doi.org/10.1029/2012JC007958

Scott, S. G., Bui, T. P., Chan, K. R., & Bowen, S. W. (1990). The meteorological measurement system on the NASA ER-2 aircraft. *Journal of Atmospheric and Oceanic Technology*, *7*(4), 525–540. https://doi.org/10.1175/1520-0426(1990)007<0525:tmmsot>2.0.co;2

Severinghaus, J. P. (1995). *Studies of the terrestrial O_2 and carbon cycles in sand dune gases and in Biosphere 2*. Columbia University.

Shulenberger, E., & Reid, J. L. (1981). The Pacific shallow oxygen maximum, deep chlorophyll maximum, and primary productivity, reconsidered. *Deep-Sea Research, Part A: Oceanographic Research Papers*, *28*(9), 901–919. https://doi.org/10.1016/0198-0149(81)90009-1

Stephens, B. B., Keeling, R. F., Heimann, M., Six, K. D., Murnane, R., & Caldeira, K. (1998). Testing global ocean carbon cycle models using measurements of atmospheric O_2 and CO_2 concentration. *Global Biogeochemical Cycles*, *12*(2), 213–230. https://doi.org/10.1029/97GB03500

Stephens, B. B., Keeling, R. F., & Paplawsky, W. J. (2011). Shipboard measurements of atmospheric oxygen using a vacuum-ultraviolet absorption technique. *Tellus B: Chemical and Physical Meteorology*, *55*(4), 857–878. https://doi.org/10.3402/tellusb.v55i4.16386

Stephens, B. B., Morgan, E. J., Bent, J. D., Keeling, R. F., Watt, A. S., Shertz, S. R., & Daube, B. C. (2021). Airborne measurements of oxygen concentration from the surface to the lower stratosphere and pole to pole. *Atmospheric Measurement Techniques*, *14*(3), 2543–2574. https://doi.org/10.5194/amt-14-2543-2021

Stephens, B., Keeling, R., Bent, J., Watt, A., Shertz, S., & Paplawsky, W. (2021a). *HIPPO-1 airborne oxygen instrument. Version 2.0*. UCAR/NCAR—Earth Observing Laboratory. https://doi.org/10.5065/D6J38QVV

Stephens, B., Keeling, R., Bent, J., Watt, A., Shertz, S., & Paplawsky, W. (2021b). *HIPPO-2 airborne oxygen instrument. Version 2.0*. UCAR/NCAR—Earth Observing Laboratory. https://doi.org/10.5065/D65Q4TF0

Stephens, B., Keeling, R., Bent, J., Watt, A., Shertz, S., & Paplawsky, W. (2021c). *HIPPO-3 airborne oxygen instrument. Version 2.0*. UCAR/NCAR—Earth Observing Laboratory. https://doi.org/10.5065/D67H1GXJ

Stephens, B., Keeling, R., Bent, J., Watt, A., Shertz, S., & Paplawsky, W. (2021d). *HIPPO-4 airborne oxygen instrument. Version 2.0*. UCAR/NCAR—Earth Observing Laboratory. https://doi.org/10.5065/D679431D

Stephens, B., Keeling, R., Bent, J., Watt, A., Shertz, S., & Paplawsky, W. (2021e). *HIPPO-5 airborne oxygen instrument. Version 2.0*. UCAR/NCAR—Earth Observing Laboratory. https://doi.org/10.5065/D6WW7G0D

Stohl, A., Bonasoni, P., Cristofanelli, P., Collins, W., Feichter, J., Frank, A., et al. (2003). Stratosphere-troposphere exchange: A review, and what we have learned from STACCATO. *Journal of Geophysical Research*, *108*(12), 8516. https://doi.org/10.1029/2002jd002490

Stull, R. B. (2012). *An introduction to boundary layer meteorology*. Springer Science & Business Media.

Sun, D., Ito, T., & Bracco, A. (2017). Oceanic uptake of oxygen during deep convection events through diffusive and bubble-mediated gas exchange. *Global Biogeochemical Cycles*, *31*(10), 1579–1591. https://doi.org/10.1002/2017GB005716

Takahashi, T., Sutherland, S. C., Wanninkhof, R., Sweeney, C., Feely, R. A., Chipman, D. W., et al. (2009). Climatological mean and decadal change in surface ocean pCO_2, and net sea-air CO_2 flux over the global oceans. *Deep-Sea Research Part II Topical Studies in Oceanography*, *56*(8–10), 554–577. https://doi.org/10.1016/j.dsr2.2008.12.009

Thompson, C. R., Wofsy, S. C., Prather, M. J., Newman, P. A., Hanisco, T. F., Ryerson, T. B., et al. (2022). The NASA atmospheric tomography (ATom) mission: Imaging the chemistry of the global atmosphere. *Bulletin of the American Meteorological Society*, *103*(3), 761–790. https://doi.org/10.1175/BAMS-D-20-0315.1

Thompson, R. L., Manning, A. C., Lowe, D. C., & Weatherburn, D. C. (2007). A ship-based methodology for high precision atmospheric oxygen measurements and its application in the Southern Ocean region. *Tellus Series B Chemical and Physical Meteorology*, *59*(4), 643–653. https://doi.org/10.1111/j.1600-0889.2007.00292.x

Tohjima, Y., Minejima, C., Mukai, H., MacHida, T., Yamagishi, H., & Nojiri, Y. (2012). Analysis of seasonality and annual mean distribution of atmospheric potential oxygen (APO) in the Pacific region. *Global Biogeochemical Cycles*, *26*(4), GB4008. https://doi.org/10.1029/2011GB004110

Tohjima, Y., Mukai, H., MacHida, T., Hoshina, Y., & Nakaoka, S. I. (2019). Global carbon budgets estimated from atmospheric O_2/N_2 and CO_2 observations in the western Pacific region over a 15-year period. *Atmospheric Chemistry and Physics*, *19*(14), 9269–9285. https://doi.org/10.5194/acp-19-9269-2019

Tohjima, Y., Mukai, H., Machida, T., & Nojiri, Y. (2003). Gas-chromatographic measurements of the atmospheric oxygen/nitrogen ratio at Hateruma Island and Cape Ochi-ishi, Japan. *Geophysical Research Letters*, *30*(12), 1653. https://doi.org/10.1029/2003GL017282

Tohjima, Y., Terao, Y., Mukai, H., Machida, T., Nojiri, Y., & Maksyutov, S. (2015). ENSO-related variability in latitudinal distribution of annual mean atmospheric potential oxygen (APO) in the equatorial Western Pacific. *Tellus Series B Chemical and Physical Meteorology*, *67*(1), 25869. https://doi.org/10.3402/tellusb.v67.25869

Tsujino, H., Urakawa, S., Nakano, H., Small, R. J., Kim, W. M., Yeager, S. G., et al. (2018). JRA-55 based surface dataset for driving ocean–sea-ice models (JRA55-do). *Ocean Modelling*, *130*, 79–139. https://doi.org/10.1016/j.ocemod.2018.07.002

Wanninkhof, R. (1992). Relationship between wind speed and gas exchange over the ocean revisited. *Limnology and Oceanography: Methods*, *97*(C5), 7373–7382. https://doi.org/10.4319/lom.2014.12.351

Weiss, R. F. (1970). The solubility of nitrogen, oxygen and argon in water and seawater. *Deep-Sea Research and Oceanographic Abstracts*, *17*(4), 721–735. https://doi.org/10.1016/0011-7471(70)90037-9

Wofsy, S. C. (2011). HIAPER Pole-to-Pole observations (HIPPO): Fine-grained, global-scale measurements of climatically important atmospheric gases and aerosols. *Philosophical Transactions of the Royal Society A: Mathematical, Physical & Engineering Sciences*, *369*(1943), 2073–2086. https://doi.org/10.1098/rsta.2010.0313

Wofsy, S. C. (2017). *HIPPO merged 10-second meteorology, atmospheric chemistry, and aerosol data. Version 1.0*. UCAR/NCAR - Earth Observing Laboratory. https://doi.org/10.3334/CDIAC/HIPPO_010

Wofsy, S. C., Afshar, S., Allen, H. M., Apel, E. C., Asher, E. C., Barletta, B., et al. (2021). *ATom: Merged atmospheric chemistry, trace gases, and aerosols, version 2 (version 2.0)*. ORNL Distributed Active Archive Center. https://doi.org/10.3334/ORNLDAAC/1925

Wofsy, S. C., Afshar, S., Allen, H., Apel, E., Asher, E., Barletta, B., et al. (2018). *ATom: Merged atmospheric chemistry, trace gases, and aerosols*. ORNL DAAC. https://doi.org/10.3334/ORNLDAAC/1581

Wofsy, S., Daube, B., Jimenez, R., Kort, E., Pittman, J., Park, S., et al. (2017). HIPPO merged 10-second meteorology, atmospheric chemistry, and aerosol data. Version 1.0 (version 1.0) [Dataset]. UCAR/NCAR—Earth Observing Laboratory. https://doi.org/10.3334/CDIAC/HIPPO_010

Worrall, F., Clay, G. D., Masiello, C. A., & Mynheer, G. (2013). Estimating the oxidative ratio of the global terrestrial biosphere carbon. *Biogeochemistry*, *115*(1–3), 23–32. https://doi.org/10.1007/s10533-013-9877-6

Yang, B., Emerson, S. R., & Bushinsky, S. M. (2017). Annual net community production in the subtropical Pacific Ocean from in situ oxygen measurements on profiling floats. *Global Biogeochemical Cycles*, *31*(4), 728–744. https://doi.org/10.1002/2016GB005545

Yeager, S. G., Rosenbloom, N., Glanville, A. A., Wu, X., Simpson, I., Li, H., et al. (2022). The seasonal-to-multiyear large ensemble (SMYLE) prediction system using the community Earth system model version 2. *Geoscientific Model Development*, *15*(16), 6451–6493. https://doi.org/10.5194/gmd-15-6451-2022

Zondlo, M. A., Paige, M. E., Massick, S. M., & Silver, J. A. (2010). Vertical cavity laser hygrometer for the national science foundation gulfstream-V aircraft. *Journal of Geophysical Research*, *115*(D20), D20309. https://doi.org/10.1029/2010JD014445